UNIVERSITY OF OKLAHOMA

GRADUATE COLLEGE

DESIGN AND PERFORMANCE EVALUATION OF A RETRACTABLE WINGTIP VORTEX REDUCTION DEVICE

A THESIS

SUBMITTED TO THE GRADUATE FACULTY

In partial fulfillment of the requirements for the

Degree of

Master of Science

Mechanical Engineering

By

Tausif Jamal
Norman, OK
2019

DESIGN AND PERFORMANCE EVALUATION OF A RETRACTABLE WINGTIP VORTEX REDUCTION DEVICE

A THESIS APPROVED FOR THE SCHOOL OF AEROSPACE AND MECHANICAL ENGINEERING

BY THE COMMITTEE CONSISTING OF

Dr. D. Keith Walters, Chair

Dr. Hamidreza Shabgard

Dr. Prakash Vedula

ABSTRACT

As an airfoil achieves lift, the pressure differential at the wingtips trigger the roll up of fluid which results in swirling wakes. This wake is characterized by the presence of strong rotating cylindrical vortices that can persist for miles. Since large aircrafts can generate strong vortices, airports require a minimum separation between two aircrafts to ensure safe take-off and landing. Recently, there have been considerable efforts to address the effects of wingtip vortices such as the categorization of expected wake turbulence for commercial aircrafts to optimize the wait times during take-off and landing. However, apart from the implementation of winglets, there has been little effort to address the issue of wingtip vortices via minimal changes to airfoil design. The primary objective of this study is to evaluate the performance of a newly proposed retractable wingtip vortex reduction device for commercial aircrafts. The proposed design consists of longitudinal slits placed in the streamwise direction near the wingtip to reduce the pressure differential between the pressure and the suction sides. This passively bled air introduces turbulent fluctuations which interact and dissipate some of the wingtip vortex strength. Results from numerical simulations performed on a NACA 0012 airfoil and a flat plate suggest that the proposed design can mitigate the strength of wingtip vortices without significant changes to existing airfoil designs with some penalty in the form of added drag and a decrease in lift. However, these inefficiencies could potentially be offset by increased air traffic via a reduction in take-off and landing wait-times. It was concluded that the proposed design reduces wingtip vortex strength and further improvements in performance could be achieved by making design adjustments to the leading edge of the airfoil where vortex generation mechanism is initiated.

ACKNOWLEDGEMENTS

I would like to thank my advisor, Dr. D. Keith Walters, for his support throughout my undergraduate and graduate career. His work ethic, enthusiasm and understanding of fluid mechanics never ceases to amaze me. I would also like to thank my co-worker and friends in our Computational Fluid Dynamics Research Team who are always supportive and invoke thoughtful conversations that challenge my understanding of fluid mechanics. Finally, I would like to thank my wife and my parents who have always been supportive of me and my work.

TABLE OF CONTENTS

LIST OF FIGURES

NOMENCLATURE

c	Chord Length
ρ	Air Density
μ	Dynamic Viscosity
U_∞	Free Stream Velocity
Re_c	Reynolds Number based on chord length
AoA	Angle of Attack
NM	Nautical Miles (1Nautical Mile = 1.15078 Miles)
RANS	Reynolds Averaged Navier-Stokes
SA	Spalart-Allmaras Model
DNS	Direct Numerical Simulation
LES	Large Eddy Simulation
HRL	Hybrid RANS-LES
DES	Detached-Eddy Simulation
DDES	Delayed Detached-Eddy Simulation
UAV	Unmanned Aerial Vehicle
y^+	Non-dimensional Wall Distance

CHAPTER I

INTRODUCTION

Flows past aircrafts and airfoils have been extensively studied since the advent of flight in the early 1900s. In the last century, significant advances in aerospace engineering has led to modern aircrafts becoming increasingly safer, faster, and efficient. Today, commercial airliners such as the Airbus A380 can carry as much as 850 passengers across the world with comfort and safety. Although modern innovations continue to push the boundaries of physics, some problems are yet to be successfully addressed. One such issue is the mitigation of wingtip vortices.

Airfoils achieve lift by creating a pressure differential between its two surfaces. This pressure differential causes the high-pressure region to push up against the lower-pressure region resulting in lift. As a result of this pressure differential, near the wingtips, flow swirls from the lower surface (pressure side) of the wing towards the upper surface (suction side) generating rotating columns of air that known as wingtip vortices as shown by Figure 1.

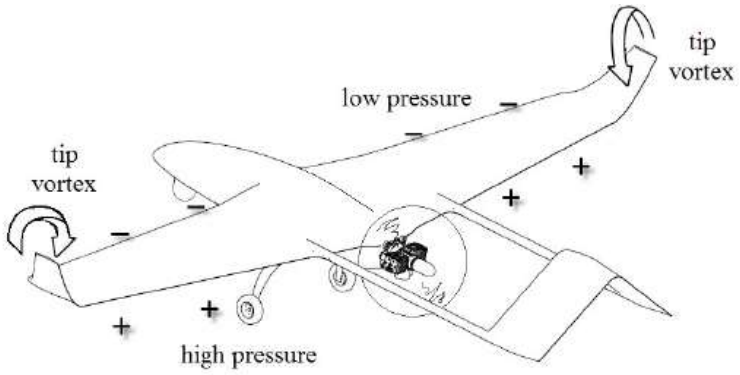

Figure 1: Wingtip vortex formation [1]

The generation of wingtip vortices is a major contributor to aerodynamic inefficiency via an increase in drag and a reduction in lift. Vortices can also cause development of unsteady loads on the lifting surfaces inducing a moment that can potentially destabilize the aircraft. Generally, the size and strength of wingtip vortices are directly proportional to the size of the lifting surface and the amount of lift generated. For large airlines, strong wingtip vortices can persist for miles downstream and are a potential hazard to any aircraft following in the wake. This wake is especially dangerous during landing and take-off when aircrafts operate at high angles of attack in a confined airspace. For example, a minimum radar separation of 4NM is required for any aircraft preceded by the Boeing 757 which can translate into 2-3 minutes of runway wait time. Efforts to address the effects of wingtip vortices include a recent re-categorization of aircraft based on expected wake turbulence, in order to optimize wait times by, for example, reducing the required wait time between smaller or slower aircraft [2]. Such an approach has been shown to improve airport operation efficiency by up to 15% [3].

Today, all the major aviation authorities such as Federal Aviation Authority and European Union Aviation Safety Agency have strict take-off and landing radar separation guidelines as a direct consequence of numerous accidents related to wake turbulence. In 2017, a Bombardier Challenger 604 was damaged beyond repair after losing an altitude of 10,000 ft as it interacted with wakes left behind by an Airbus A380 over the Arabian Sea [4]. On June 14th 2018, Qantas Flight QF94 suffered a ten second freefall after take-off caused by the wakes of the preceding Qantas Flight QF12 which departed two minutes earlier [5]. Although, there have been numerous efforts to reduce the effect of the wakes caused by these wingtip vortices, accidents caused by wake induced turbulence still occur today. Hence improvements in airfoil design is an important avenue of active research in industry and academia. The present generation of wingtip devices

have improved aerodynamic efficiency considerably, some estimates indicate an overall improvement in aerodynamic efficiency of about 4% to 5% [6] which results in enormous fuel savings worldwide. However, with the exception of winglets, which have been adopted for regional and long-range commercial aircraft, there has been relatively little effort to address wingtip vortices via changes in wingtip design.

This thesis evaluates the performance of a proposed retractable wingtip vortex reduction device to reduce wait times between successive take-offs and landings. Since the formation of wingtip vortices depend on the pressure gradient, it is possible to reduce the strength of the vortex by bleeding air through the airfoil. To achieve this goal, slits in the streamwise direction were implemented into the baseline airfoils and results were evaluated using high fidelity Computational Fluid Dynamics (CFD). Numerical simulations were performed using Large Eddy Simulation for a NACA0012 and a flat plate with the proposed design. Results indicate that the implementation of slits interrupts the formation of a coherent wingtip vortex. Although some aerodynamic losses are observed, the increased cost could potentially be offset by an increase in the number of flights.

CHAPTER II

LITERATURE REVIEW

Effective methods for wingtip vortex mitigation have found practical use in aviation as early as in 1910 when W.E. Sommerville patented the first known functional winglets. Since then there has been significant effort to implement efficient and effective wingtip vortex mitigation devices [7]. In early 1970, NASA Langley conducted several investigations of a wingtip design and configuration in a response to the rising fuel costs and the subsequent fuel crisis of 1973. Their investigations indicated that correctly angled winglets could maintain same or lower bending moment with a smaller wingspan and have greater flight stability than tip extensions. Their designs were eventually implemented in the McDonnel Douglas MD-11 and NASA's 747 space shuttle carrier [8]. Since then, most of the experimental work has focused primarily on development of wingtip devices for increased efficiency and there is a lack of studies targeted solely towards vortex mitigation.

The following sections detail relevant experimental and numerical contributions in the area of wingtip vortex identification and mitigation.

2.1 Experimental Studies

Patterson [9] carried out experimental studies at NASA Langley Research Center to determine if a drogue device positioned downstream the wingtip can be used to successfully breakdown vortices. The experimental setup consisted of scale models mounted on rails and driven through a test section containing smoke where cameras were used to photograph the flow. The results indicated that the introduction of a drogue or spline device for a preceding aircraft would reduce the induced roll for the trailing aircraft. Following the experiments, real-world tests were

conducted using the spline on a Douglas C-54 which was followed by a Piper Cherokee aircraft. Although rolling moment experienced by the following aircraft was significantly decreased, the author indicated that there was an increase in take-off distance and a reduction in the rate of climb. Ultimately, the author concluded that wingtip vortices can be attenuated to a large degree by affecting the pressure field downstream of the vortex and that vortex attenuation similar to a spline device could also be achieved by directing high-energy jet engine wake into the vortex core.

In 1980, Smith [10] suggested the use of porous wingtips to reduce the pressure differential at the wingtip. In the study conducted by the author, porous wingtips with a porosity of 10% were designed and implemented on a Cessna 0-1. Results indicated a reduction in maximum tangential velocity without a significant increase in induced drag. The 10% porous wingtip showed up to 60% reduction in trailing vortex within 1c behind the wing. The author concluded that a porous wing is a relatively effective method of wingtip vortex reduction without any negative impacts on the aerodynamic performance of the wing. Although no detailed study was carried out on the drag characteristics, the authors suggested that mechanically adjusting the porosity during flight could help reduce drag.

Wind-tunnel experiments to better understand the behavior and structure of the wingtip vortex generated by a NACA 0015 airfoil at three AoA (4° ,8°, and 12°) were carried out by Anderson et al. [11]. The wind tunnel test data was measured at three spanwise locations, x/c=-0.2, 0.05, and 0.1 from the trailing edge at a Re_c of $1x10^6$ using triple-sensor hot wire probe and titanium tetrachloride smoke injection. Results indicated that the development and the structure of the vortex is strongly influenced by the AoA and the end cap treatment of the wing section. For flat end-cap wingtip, multiple vortices were observed forming near the leading edge of the wingtip and merging downstream of the wing. The location where these vortices merged and the number

of vortices generated, progressively increased with an increase in the AoA. For round end-cap wingtips, a single coherent vortex formation was observed for all three AoA. In contrast to the flat end-cap results, the single vortex observed in round end-cap case was characterized by higher tangential velocity which ultimately resulted in a stronger vortex. The authors concluded that energy is lost for the flat end-cap wings and distributed to multiple vortices that do not have a common center of rotation when compared to the round end-cap wings and that further studies with higher resolution imaging needs to be carried out in order to better understand the flow behavior as it interacts with wing.

Recently, Guha [12] investigated the performance of a Macro-Fiber Composite Piezoelectric Actuated Winglet as a means to reduce wingtip vortices. Performance of two winglets with dihedral orientations of 0° and 75° were studied using Stereoscopic Particle Image Velocimetry (SPIV). The winglets were oscillated using an actuator with a sinusoidal input. Results indicated that the vortex core developed at the root of the winglet with vorticity peaks occurring at the root, middle and tip of the winglet. The winglet oscillations also introduced perturbations in the flowfield that successfully diffused the wingtip vortex. The author concluded that smart materials maybe used to develop active wingtip devices such as rakes, fences and multiple wingtips to help mitigate the strength of wingtip vortices.

Altaf [13] carried out wind-tunnel tests for a reverse delta type add-on device as a wingtip vortex mitigation device using a half span model at High Lift Configuration at a Re_c of $2.75x10^5$. Wind tunnel tests using Particle Image Velocimetry (PIV) and charge couple device (CCD) cameras were used to determine the effectiveness of the design. The results indicated a considerable reduction in tangential velocity and vorticity caused by the interaction of the wake from the wingtip and the add-on device. However, aerodynamic losses in the form of increased

drag and reduced lift was also observed. According to the author, several outstanding issues remained. Further studies to determine the immediate aerodynamic effect of the delta being deployed in flight or in a wind tunnel, performance of the delta device at a combination of roll and pitch angles for multi-element wings, and studies related to different structural configurations need to be carried out to further validate the performance of the delta add-on device.

2.2 Numerical Studies

Numerical studies of flow over a NACA0012 at Re_c of $1.2x10^6$ were carried out by Lombard et al. [14] using Spectral Vanishing Viscosity-implicit LES (SVV-iLES) and validated against experimental data. The study was primarily aimed at successfully resolving the complex flow physics associated with airfoils at high Reynolds number using LES. Results from the study indicated that SVV-iLES has the potential to resolve complex turbulence without the use of explicit sub-grid scale models. The model showed improved correlation with experimental studies for coefficient of pressure profiles, axial velocity and the position of the vortex core. However, some discrepancies were observed with the position of the suction peak which appeared further downstream than in experimental studies. In summary, the authors concluded that SVV-iLES is a useful tool to compute vortex dominated unsteady flows in aerospace applications.

Jamal et al. [15] investigated the performance of RANS and hybrid RANS-LES models for flow in a vortex cell. Suggested by Ringleb [16] in 1961, the idea of a vortex cell revolves around successfully trapping a vortex in a control surface to achieve favorable interaction with the boundary layers and to prevent the mechanism of vortex shedding. Results indicated a general qualitative agreement with experimental data with errors in velocity predictions caused by overexaggerated turbulent mixing form the RANS model in the dynamic Hybrid RANS-LES model. The authors concluded that several key deficiencies need to be addressed before the

complex flows can be successfully simulated using RANS and hybrid RANS-LES models. Most importantly, there is a need for better RANS models and/or RANS to LES transition parameters.

2.3 Outstanding Issues

The articles mentioned in the previous sections show that most investigations related to wing-tip vortices is still ongoing with numerical studies still in their infancy and require improved modeling techniques. As suggested by Lombard et al. [14], the issue of vortex structure is not well understood therefore turbulence modeling is difficult as it is a daunting task to determine appropriate model constants in order to successfully model these flows. The vortex cell study in [15] supported this argument. Industry standard models that have been verified and benchmarked numerous times failed to produce accurate predictions highlighting some of the difficulties associated with turbulence modeling of complex vortex shedding. Also, most studies focus on improving aerodynamic efficiency while the issue of reducing wait times between successive flights is rarely investigated. This thesis attempts to lay the foundation for future developments by showcasing some of the challenges associated with simulating advanced airfoil configurations in addition to proposing an effective wingtip vortex reduction device.

CHAPTER III

TURBULENCE MODELING & NUMERICAL METHODS

Flows around aircrafts and airfoils are characterized by high Reynolds numbers, unsteady wakes, vortex shedding and complex interactions. Due to these complexities, numerically solving these flows is notoriously difficult. Even today, wind tunnel tests form the backbone of development and verification of aerodynamic design. With an increase in computing power and with improved turbulence models, numerical methods used in design and analysis have started to gain traction. Methods such as CFD have the capability to substantially reduce the cost and effort required for the development and analysis of aerodynamic designs. However, successful CFD simulation of complex designs presents its own set of challenges. Because most CFD simulations of complex turbulent flows involve the use of turbulence models and complex geometries, proper selection of these models, boundary conditions, and a rigorous knowledge of the underlying flow physics is necessary to accurately perform any numerical evaluation.

The following sections will introduce some of the techniques used in this study.

3.1 Turbulence Modeling Basics

In most industrial engineering flows, a complete description of all the flow physics is not always required. Rather, a mean description of the flow is sufficient to perform engineering design and validation. On the other hand, for some aerospace and research applications, a more in-depth knowledge of the flow with an accurate description of the interaction of different scales of motion is required. The following sections will briefly discuss the two main approaches used in modern CFD simulations.

3.2 Reynolds Averaged Navier-Stokes (RANS)

RANS based turbulence models are perhaps one of the most commonly used CFD models used in the industry today. The RANS modeling approach involves solving the Navier-Stokes equations for an averaged description of the flowfield while the effects caused by complex fluctuations are included via transport equations based on statistical quantities. RANS models are also relatively insensitive to the CFD mesh topology (structured, unstructured or hybrid) and grid independent results can generally be obtained in a straightforward manner. However, because they only resolve the mean flowfield and rely on significant empiricism in the modeled terms, RANS models are known to perform less reliably for complex flows such as separated shear layers, flows with adverse pressure gradients, and large-scale unsteadiness.

The Navier-Stokes mass and momentum conservation equations for an incompressible fluid are given below :-

$$\frac{\partial u_i}{\partial x_i} = 0 \tag{1}$$

$$\frac{\partial u_i}{\partial t} + u_j \frac{\partial u_i}{\partial x_j} = -\frac{1}{\rho}\frac{\partial p}{\partial x_i} + \mu \frac{\partial^2}{\partial x_j \partial x_j} u_i + gz + f_i \tag{2}$$

where u_i is the velocity vector, p is pressure, ν is the kinematic viscosity, gz is the body force (gravitational force or electromagnetic force), and f_i is a source term. For simplification we can neglect the last two terms when deriving the RANS equations for the present study.

The RANS approach decomposes the velocity field into the sum of mean and fluctuating components as shown in Equation 3.

$$u(x,t) = \underbrace{\overline{U}(x,t)}_{mean} + \underbrace{u'(x,t)}_{fluctuating} \tag{3}$$

Once substituted into the Navier-Stokes equations and ensemble-averaged, the RANS equations are obtained as shown in Equation 4 and 5. The overbar denotes averaged quantities.

$$\frac{\partial \bar{U}_i}{\partial x_j} = 0 \tag{4}$$

$$\frac{\partial \bar{U}_i}{\partial t} + \bar{U}_j \frac{\partial \bar{U}_i}{\partial x_j} = -\frac{1}{\rho}\frac{\partial \bar{P}}{\partial x_i} + \mu \frac{\partial^2 \bar{U}_i}{\partial x_j \partial x_j} - \frac{\partial \overbrace{\widetilde{u_j u_i}}^{Reynolds\ Stress}}{\partial x_j} \tag{5}$$

These two equations represent the RANS mass and momentum conservation equations. The additional term in Equation 5, known as the Reynolds stress, is the bi-product of the ensemble-averaging process which describes the interaction of mean and fluctuating scales of motion. RANS models solve for additional equations to approximate the Reynolds stress term in order to close the equation

Numerous studies have been performed validating the performance of RANS based models for a range of different engineering flows. Since RANS methods model all scales of turbulent motion, their relatively low computational requirement and ease of use make them an industry staple. It has also been shown that RANS models are able to represent near wall flow physics with considerable accuracy due to the universality of the flow in the boundary layer. For more complex flows such as transition and separated turbulent flows, three and four equation RANS models have also been successfully employed.

3.2.1. Splart-Allmaras (SA) Model

The Spalart-Allmaras or the SA model [17] is a one-equation turbulence model widely used for aerodynamic applications. The model transport equation is solved for the kinematic eddy viscosity which serves as a closure for the RANS equations. The SA model has been validated for

a variety of different flow problems involving wall-bounded flows and boundary layers subjected to adverse pressure gradients. The model transport equation for eddy viscosity is given by :

$$\frac{D\rho\tilde{\nu}}{Dt} = G_\nu - Y_\nu + \frac{1}{\sigma_{\tilde{\nu}}}\left[\frac{\partial}{\partial x_j}\left\{(\mu + \rho\tilde{\nu})\frac{\partial\tilde{\nu}}{\partial x_j}\right\} + C_{b2}\rho\left(\frac{\partial\tilde{\nu}}{\partial x_j}\right)^2\right] + S_{\tilde{\nu}} \tag{6}$$

$$G_\nu = C_{b1}\rho\tilde{S}\tilde{\nu} \tag{7}$$

$$Y_\nu = C_{\omega 1}\rho f_\omega \left(\frac{\tilde{\nu}}{d}\right)^2 \tag{8}$$

where G_ν and Y_ν are the production term and the destruction terms respectively. $\sigma_{\tilde{\nu}}$ and C_{b2} are the constants, while ν is the molecular kinematic viscosity and $S_{\tilde{\nu}}$ is a user-defined source term.

3.3 Large Eddy Simulation (LES)

In the last decade, LES has gained significant prominence in simulating complex three-dimensional flows where RANS model performance has been found to be inadequate. In flows involving complex interactions between different scales of motion and in separated shear layers, LES models have been found to perform better than existing RANS models. The fundamental idea behind LES models relies on separating the large energy-carrying scales from the dissipative scales of motion. Filters are applied to the Navier-Stokes equations where large turbulent structures are resolved while, the smaller scales are represented using a subgrid scale (SGS) model. LES models perform well where large eddies dictate the energy and momentum transfer. But despite their advantages, LES models are computationally expensive compared to RANS and are not very common in general industrial applications.

The LES approach separates the flow into resolved and unresolved scales of motion as shown in the following equation where the tilde (~) operator represents filtered quantities.

$$\tilde{u}(x,t) = \underbrace{U(x,t)}_{resolved} + \underbrace{u(x,t)}_{unresolved\ scales} \tag{9}$$

Once substituted into the Navier-Stokes equations, filtered LES equations are obtained. Equations 10 and 11 represent the filtered Navier-Stokes equations for mass and momentum conservation of an incompressible fluid.

$$\frac{\partial \tilde{u}_i}{\partial x_i} = 0 \tag{10}$$

$$\frac{\partial \tilde{u}_i}{\partial t} + \tilde{u}_j \frac{\partial \tilde{u}_i}{\partial x_j} = -\frac{1}{\rho}\frac{\partial \tilde{p}}{\partial x_i} + \mu \frac{\partial^2}{\partial x_j \partial x_j}\tilde{u}_i + \frac{\partial \overbrace{\widetilde{u_i u_j}}^{\substack{Sub-filte \\ Stress}}}{\partial x_j} \tag{11}$$

Similar to the Reynolds Stress term in the RANS equations, the additional sub-filter stress term in Equation 11 is a bi-product of the filtering process which describes the interaction of resolved and unresolved scales of motion. The sub-filter stress term is modeled for closure of the momentum equations.

3.3.1 Hybrid RANS-LES (HRL)

The HRL modeling approach aims to provide the best of both worlds, the accuracy of LES coupled with the efficiency of RANS. In HRL modeling, near-wall regions with universal wall bounded turbulence are treated using an SGS (Sub-Grid Scale) model or a RANS model while, large scale structures primarily responsible for the transfer of momentum and energy are explicitly solved by LES. Traditionally, the transition parameters include some ratio of turbulent length scale to local grid scale or a distance function to determine where the models transition from RANS to LES. Although these models have had considerable success in predicting complex flow features where traditional RANS models have failed, the RANS to LES transition parameters introduce a

fair share of issues. Sudden changes in grid size or aspect ratio have led to non-physical RANS to LES transition in regions where the grid is not refined enough to resolve turbulent fluctuation. Grid induced transition presents a major hurdle for tradition HRL models and several attempts have been made to address this issue such as the development of the DDES by Spalart [18].

3.3.2 Detached Eddy Simulation (DES)

DES [19] was formulated to address some of the difficulties arising from using LES methods in an explicit framework. The model traditionally transitions between a RANS model in the near-wall region to an LES model away from the walls where the grid can sufficiently resolve turbulent fluctuations. This transition is achieved by using a blending function which modifies the wall-distance in the baseline SA model. The blending function is given by :

$$\tilde{d} = \min(d, C_{DES}\Delta) \tag{12}$$

$$\Delta = \max(\Delta x, \Delta y, \Delta z) \tag{13}$$

where $\tilde{d}$ is the modified distance function, d is the nearest distance to a wall used in the SA model, C_{DES} is a calibration constant, and Δ is the largest dimension of the local grid spacing.

3.3.3 Delayed-Detached Eddy Simulation (DDES)

Proposed by Spalart et al. [18], the DDES model addresses some of the issues with DES such as shear stress depletion and grid induced separation. For traditional grids with stretched cells near the wall and in the boundary layer, the DES model ensures RANS mode when grid scale is sufficiently smaller than DES length scale. For grid scales larger than DES length scale, the model effectively transitions to LES. However, when the grid scale is comparable to DES length scale, LES mode can be incorrectly activated in the boundary layer when the grid is not sufficiently

refined to sustain the LES turbulent fluctuations. The DDES model addresses this issue by redefining the DES length scale $\tilde{\boldsymbol{d}}$ in the following equation:-

$$\tilde{d} = d - f_d \max(0, d - C_{DES}\Delta_{max}) \tag{14}$$

$$f_d = 1 - \tanh((8r_d)^3) \tag{15}$$

$$r_d = \frac{\tilde{\nu}}{\sqrt{U_{i,j}U_{i,j}}\kappa^2 d^2} \tag{16}$$

$$\tilde{\nu} = \nu_t + \nu \tag{17}$$

where $\boldsymbol{\nu_t}$ is the eddy viscosity, ν is the molecular viscosity, $\boldsymbol{U_{i,j}}$ is the velocity gradients, κ is the Kármán constant, and d is the distance to the nearest wall.

3.3.4 Monotonically Integrated Large Eddy Simulation (MILES)

Proposed by Fureby and Grinstein [20], the MILES approach utilizes the inherent dissipative nature of finite volume methods to numerically model the effect of subgrid scales of motion on the resolved (large) scales. The MILES approach therefore contains no explicit subgrid stress model. This results in an approach that effectively resolves scales larger than the local grid scale. For this study, the MILES approach was implemented by simply running the simulation with no turbulence model.

3.4 Low Dissipation Upwind Flux Formulation (OGRE)

The Optimization-based Gradient RE-construction (OGRE) scheme is a low-dissipation numerical scheme that uses a face variable reconstruction method based on iterative least-square gradient computation to minimize 2nd order dissipation on structured grids. The scheme preserves

local monotonicity using a slope-limiter while, the left and right face states are calculated using Mach-number-weighted averaging. The scheme calculates an initial gradient given by :-

$$\frac{\partial \widehat{\phi}}{\partial x_i} = \sum_{n=1:N} \omega_{i,n}(\phi_n - \phi_0) \tag{18}$$

where ϕ is the variable, ω_i is the weight co-efficient, ϕ_n is the neighboring cell variable value of the variable ϕ, ϕ_0 is the present cell variable value, and N is the summation over the neighboring cells. Following the initial gradient calculation, a second gradient is calculated using identical weight coefficients as shown by :-

$$\frac{\partial \phi}{\partial x_i} = \sum_{n=1:n} \omega_{i,n} \left[(\phi_n - \phi_0) + 0.5 \left(\frac{\partial \widehat{\phi}}{\partial x_i}\Big|_0 - \frac{\partial \widehat{\phi}}{\partial x_i}\Big|_n \right) r_{j,0n} \right] \tag{19}$$

$\frac{\partial \widehat{\phi}}{\partial x_i}\Big|_0$ and $\frac{\partial \widehat{\phi}}{\partial x_i}\Big|_n$ are the initial cell gradients for the cell and its neighbor, variable $r_{j,0n}$ is the direction vector pointing to each neighboring cell centroid, and $\omega_{i,n}$ is the weight co-efficient. The OGRE scheme has shown to reduce numerical dissipation where any kind of cell stretching is involved for complex turbulent flows. Readers are referred to [21] for further details.

CHAPTER IV

PERFORMANCE EVALUATION USING NACA 0012

There have been several attempts at implementing devices to mitigate some of the effects of wing-tip vortices. Some changes to the existing wing design include blended wings, extrusions, turbines to extract energy, but not all of these designs have been demonstrably effective. Most of these designs permanently alter the structure of the original wing which impacts not just takeoff and landing conditions, but also free flight. The proposed design consists of a retractable section of the wing integrated internally, consisting of longitudinal apertures to reduce the pressure differential between the pressure and suction sides of the airfoil. The apertures also cause the formation of multiple, small trailing vortices which generate turbulence to effectively dissipate the formation of a coherent vortex.

To evaluate the proposed design, initial numerical studies were carried out using a NACA 0012 airfoil as discussed in the following sections.

4.1 Geometry - NACA 0012 Airfoil

The NACA 0012 is a widely used symmetric airfoil popular among UAV, gliders, and in helicopter rotors. Figures 3 (a) and (b) show a baseline NACA 0012 airfoil and the NACA 0012 airfoil with streamwise slits. The slits were originally placed starting at 50% span with increasing widths of 0.1c, 0.125c, 0.15c, 0.175c, and 0.2c towards the wingtip.

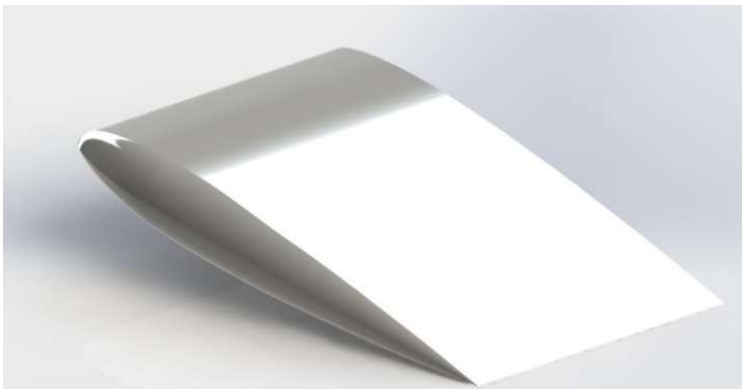

Figure 2: NACA 0012 airfoil

Figure 3: Modified NACA 0012 airfoil with slits

4.1.1 Mesh

Initially a multi-block structured grid was generated with 10.8 million tetrahedral cells. Figure 4 (a) and (b) shows the multi-blocks and the cell resolution around the airfoil.

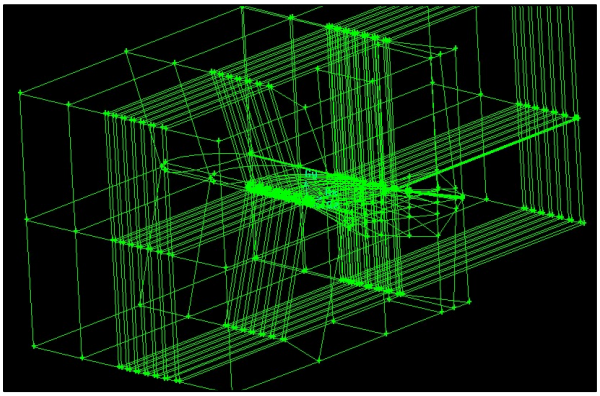

(a)

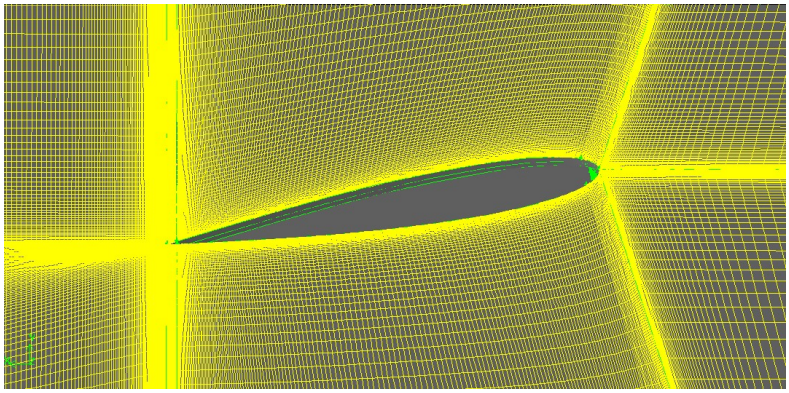

(b)

Figure 4: (a) Multi-blocks of the structured grid and (b) mesh resolution around the airfoil

Because of the convexity of the wingtip, cells in that region were highly skewed and required multiple blocks to ensure appropriate cell growth and to preserve a low aspect ratio. Even after multiple targeted refinements, the grid had high aspect ratio cells near the wingtip. To overcome the issue of highly stretched cells and to reduce computational effort, an unstructured grid was generated with approximately 5.9 million cells with a first cell height of $1x10^{-5}$ m which translated to y^+ value of 1.4. The computational domain used in this study extended 8c in the x-

direction, 5c in the y-direction and 2c in the z-direction. Figure 5 (a) and (b) show the mesh distribution around the airfoil and inside the domain.

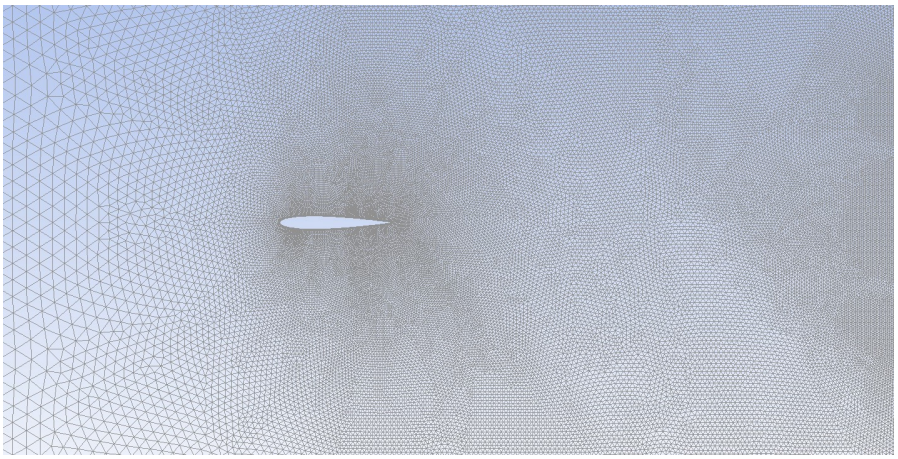

(a)

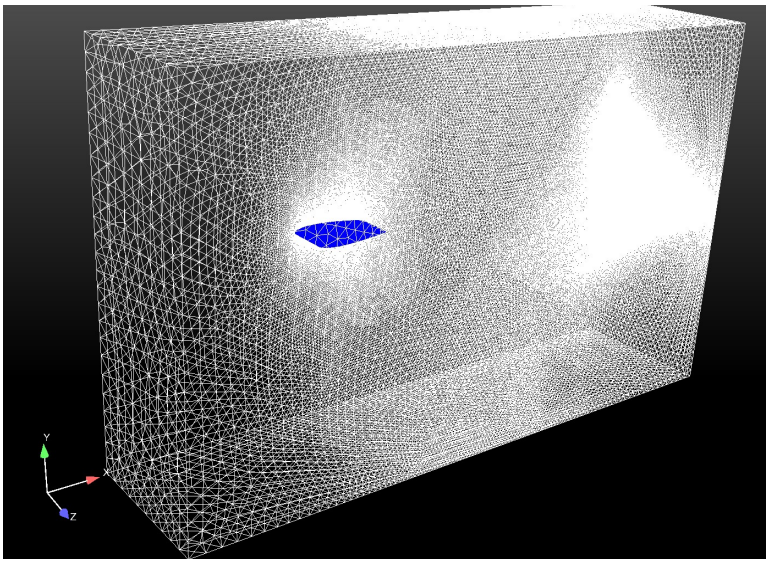

(b)

Figure 5: (a) Mesh distribution around the airfoil and (b) meshed domain

4.2 Numerical Setup

In an attempt to reduce computational effort while resolving the larger energy-carrying scales of motion, the SA-DDES HRL model was used. The SA model simulated the near wall turbulence in a linear eddy-viscosity or RANS framework in which the effect of turbulent mixing is included via an increase in the effective diffusion rate of momentum, while the DDES framework allowed the model to transition to LES mode away from the airfoil to resolve the large-scale structures.

Unsteady numerical simulations of flow over two variants of the NACA 0012 airfoil for a single-phase incompressible fluid were carried out using the SA-DDES HRL model in a pressure based finite volume double precision 3-D commercial flow solver ANSYS FLUENT® [22] with a time-step size of $1x10^{-4}$. No slip boundary condition was specified at the walls, with velocity components specified at the inlet boundary and atmospheric pressure specified at the outlet. Convective terms in the momentum equation were discretized with the Second Order scheme, while pressure and velocity were coupled with the SIMPLE algorithm, and the Standard scheme was used to discretize the pressure. The initial conditions used in the simulations are shown in Figure 6 below.

Re_c	**AoA**	**Turbulence Intensity**	**c**	**μ**	**U_∞**	**ρ**
$3.36x10^6$	10°	1%	1.009 m	$1.794x10^{-5}$ kg/m-s	50 m/s	1.225 kg/m^3

Figure 6: Table of inlet and initial conditions for NACA 0012 simulations

4.3 Results

ANSYS FLUENT® was used to run all the simulations while data was postprocessed in Paraview [23]. Figures 7, 8, and 9 show contours of Q-criterion, x-velocity fluctuation, and normalized streamwise velocity for the baseline NACA 0012 and the modified design. In Figure

7 (a), the presence of a coherent vortex generated at the wingtip is observed. The flow is also characterized by the lack of any significant turbulent fluctuations or rotations. On the other hand, Figure 7 (b) is characterized by the presence of large amounts of turbulence which effectively disrupts the formation of a coherent vortex and helps to diffuse momentum and energy more effectively. Also, the modified design exhibits a lower higher co-efficient of pressure near the leading edge compared to the baseline design signifying a decrease in pressure differential as a direct consequence of the slits.

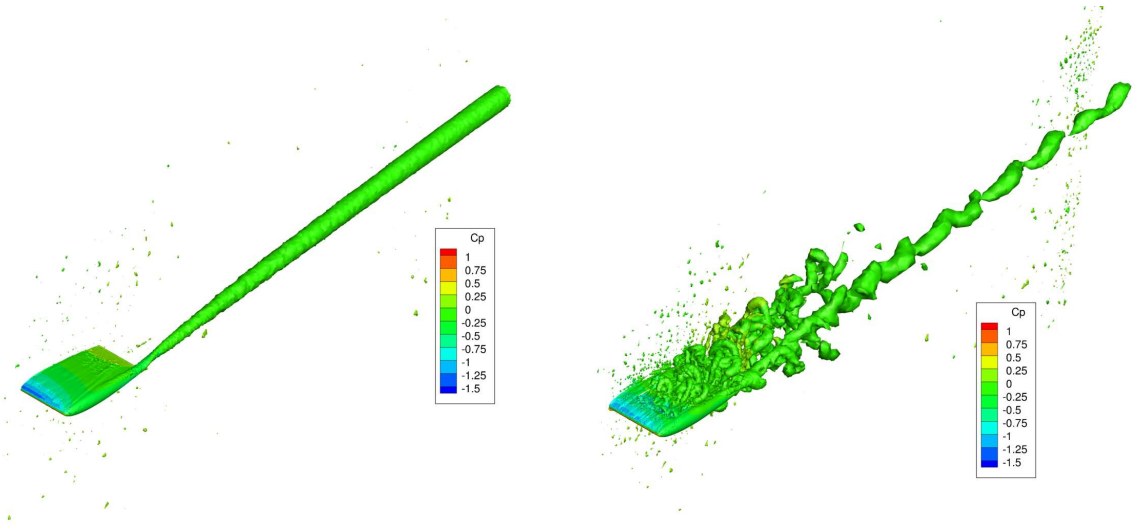

(a) (b)

Figure 7: Iso-volumes of Q-criterion colored by Cp for (a) NACA 0012 and (b) NACA 0012 with slits

Figures 8 and 9 show streamwise velocity fluctuation and normalized streamwise velocity for the two cases considered in this study. In both cases, the baseline NACA 0012 showed a lack of fluctuations with smooth and smeared flow features while the modified design showed the presence of only large-scale fluctuations around the airfoil. It was suspected that the unstructured grid topology was unable to resolve the small-scale fluctuations accurately and still contained high-

aspect ratio cells. These high aspect-ratio cells are a common source of numerical dissipation and can lead to non-physical RANS-LES transition or the suppression of LES mode altogether via the dissipation of turbulent fluctuations. Figures 7 (a) and (b) support this by indicating the presence of small spots of high Q-criterion throughout the domain further. It was concluded that for the baseline NACA 0012 case, the SA model never transitioned to DDES mode while the modified case exhibited features associated with enhanced numerical dissipation.

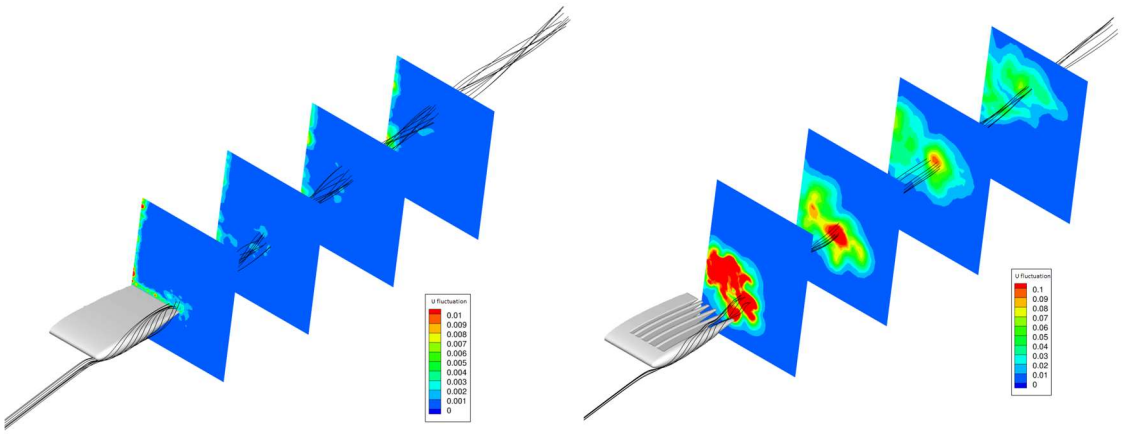

(a) (b)

Figure 8: Contours of x-velocity fluctuation for (a) NACA 0012 and (b) NACA 0012 with slits

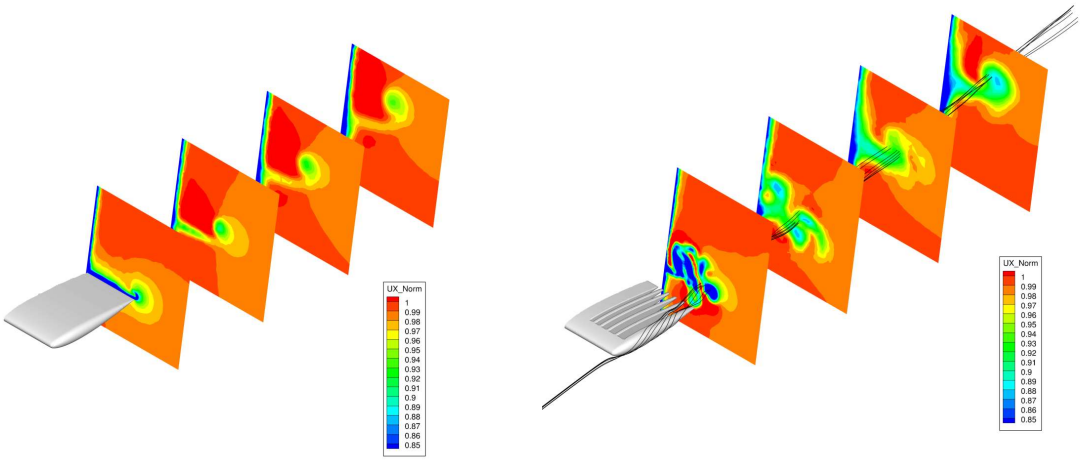

(a) (b)

Figure 9: Normalized x-velocity for (a) NACA 0012 and (b) NACA 0012 with slits

Lift and drag data indicated an overall 60% increase in drag and a 40% decrease in lift for the modified design. Although it seemed like the design was severely inefficient, the present study only simulated a small section near the wingtip of the airfoil to reduce computational cost. It is expected that simulations of an airfoil with larger wingspan would be a more accurate indicator of aerodynamic performance. Also, the slits would only be functional during take-off and landing for a few seconds. In that short time of operation, any reduction in aerodynamic efficiency could potentially be offset by a reduction in wait times.

4.4 Conclusion

The initial study established a proof-of-concept for the effectiveness of the streamwise slit configuration. Although there were some issues related to numerical dissipation, increased drag, and a loss of aerodynamic lift, the modified design indicated that it was able to disrupt the formation of a coherent vortex. It was deemed that further studies with high fidelity numerical methods was needed to appropriately determine the performance of the proposed design and to describe the mechanism of vortex generation and diffusion more accurately. Following this study,

numerical simulation of flow in a vortex cell in [15] suggested some of the shortcomings of RANS and hybrid RANS-LES models in accurately predicting the flow physics related to vortices. It was decided that for future studies a more robust modeling methodology would be needed to accurately evaluate the performance of integrated slits on an airfoil.

CHAPTER V

PERFORMANCE EVALUATION USING A FLAT PLATE

As described in the previous section, initial numerical simulations using a NACA0012 airfoil indicated the difficulties involved in accurately modeling the complex flow physics associated with wingtip vortices. Although the study indicated that the slit configuration was successfully breaking up wingtip vortices, significant aerodynamic losses were observed. Also, it was difficult to determine if the increase in losses were primarily due to airfoil design or numerical and modeling errors. Hence, it was concluded that a more robust numerical approach would be required to accurately demonstrate the effect of the proposed design.

To validate the performance of the wingtip vortex mitigation device, it was determined that high-resolution numerical scheme along with a structured grid would be necessary. To achieve these goals, CFD simulations of flow over a flat plate using MILES with a low-dissipation scheme were performed for take-off and landing speeds.

5.1 Geometry

As indicated in the previous chapter, using the NACA 0012 airfoil introduced a few grid generation challenges. To bypass those complexities, the baseline geometry was simplified to a flat plate with no thickness. This offered more control over cell distribution and made it relatively easier to generate high quality structured grids with low cell skewness. Also, for this study, four different airfoil designs were considered: i) baseline airfoil, ii) airfoil with winglet, iii) airfoil with slits, and iv) airfoil with slits and winglets as shown in Figures 10 and 11.

(a) (b)

Figure 10: Geometry of (a) flat plate and (b) flat plate with winglet

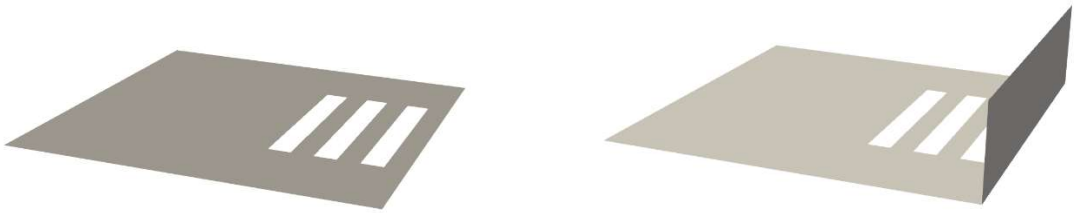

(a) (b)

Figure 11: Geomerty of (a) flat plate with slits and (b) flat plate with slits and winglet

The slits integrated into the baseline flat plates in this study are 0.0625c wide and 0.25c long beginning at 0.625c from the root in the spanwise direction while the height of the winglet is 0.25c. Figures 12 (a) and (b) shows the computational domain and the boundary conditions for this study. The new domain extends to 1c in front and 10 c behind the airfoil in the streamwise direction, 2c in the spanwise direction, and 2c in each of the airfoil normal directions. Velocity inlet and pressure outlet boundary conditions were applied in the streamwise direction along with periodic and symmentry boundary conditions applied in the airfoil-normal and spanwise directions respectively.

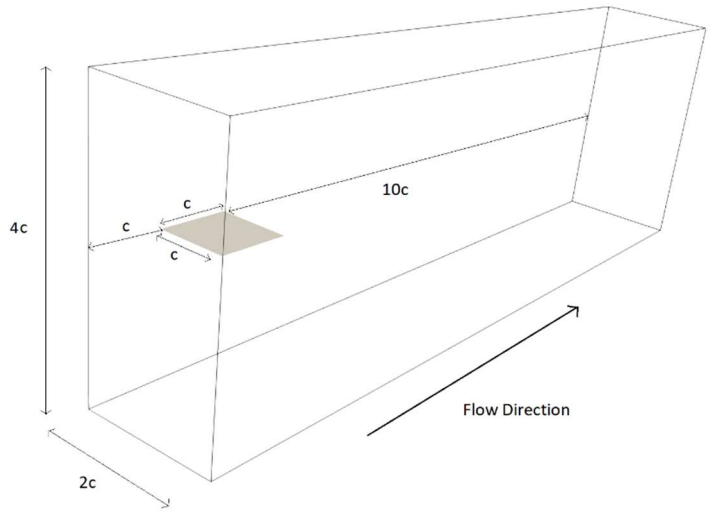

(a)

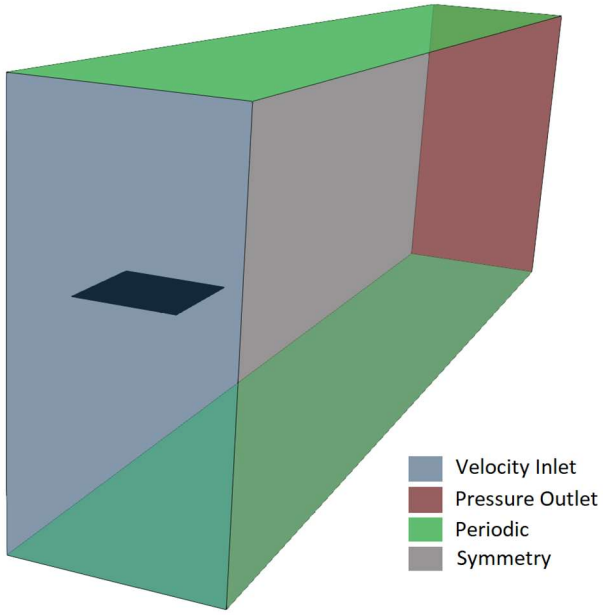

(b)

Figure 12: (a) Domain used in the study and (b) boundary conditions

5.1.1 Mesh

Initially, a coarse grid containing approximately 10 million cells was generated in Ansys and results were analyzed. Initially, a first cell height of $1x10^{-5}$ m was used which resulted in a y^+ value of 1.75. This however caused streched cells in the streamwise direction just aft of the airfoil. Since the flow over the airfoil at an AoA of 10° is already separated, there was no additional advantage in resolving the boundary layer with high cell density. The first cell height was increased to $5x10^{-4}$ m which resulted in a y^+ value of 87. The reduced cell density near the airfoil allowed for a more well resloved region behind the airfoil.

As discussed in chapter VI, some discrepancies including the presence of numerical artifacts and increased vortex strength for some of the airfoils prompted the need for a higher resolution mesh. Fine grids containing 15 million cells was generated using targeted grid refinement around the wingtip and the vortex path as indicated by the coarse grid results. Figures 13, 14 and 15 compare the resolution of the two grids used in this study.

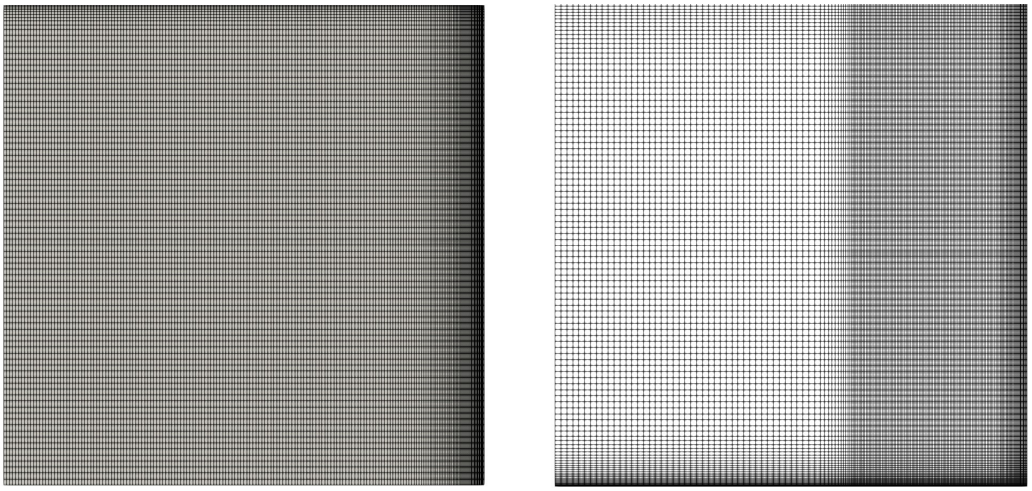

(a) (b)

Figure 13: Top view of the mesh for the (a) coarse grid and (b) fine grid

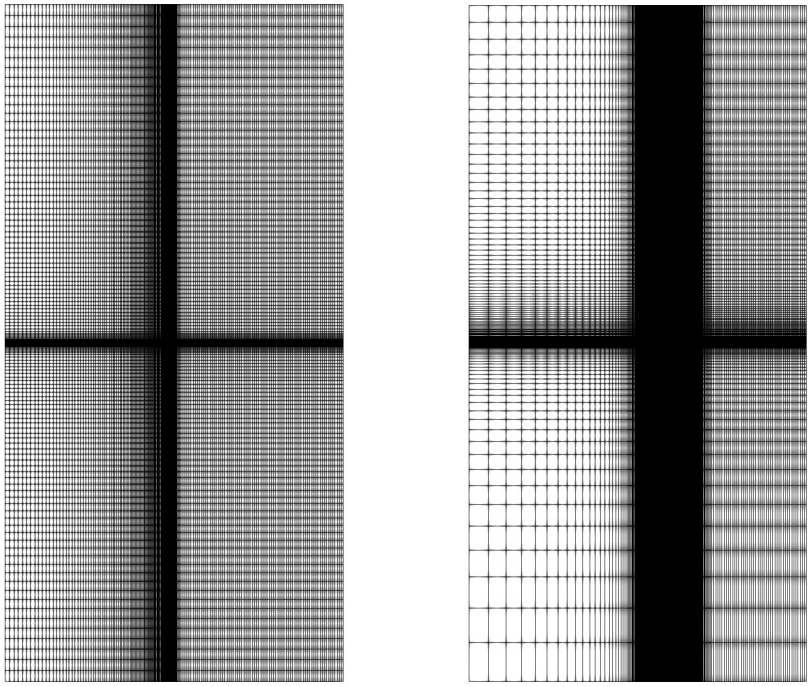

(a) (b)

Figure 14: Front view of the inlet boundary for the (a) coarse grid and (b) fine grid

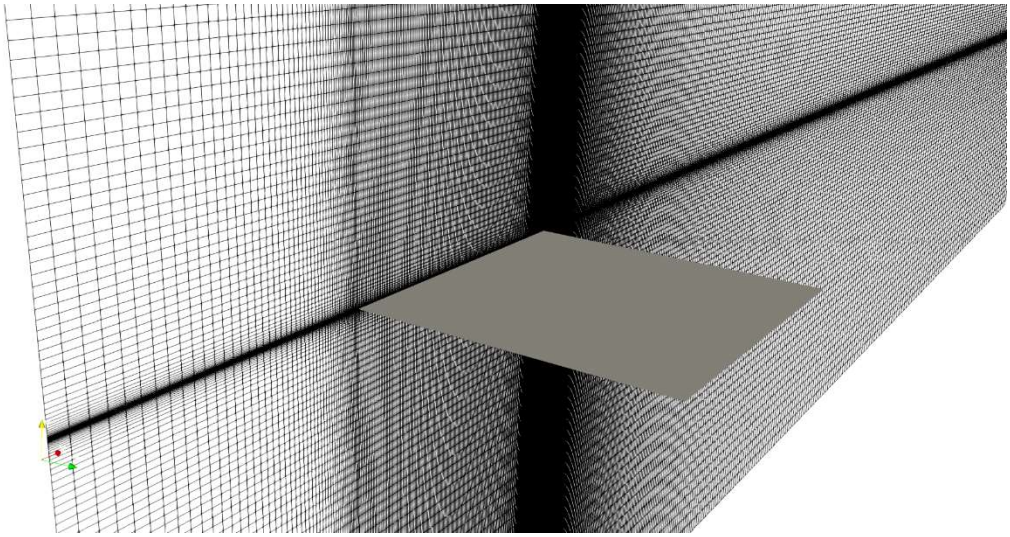

(a)

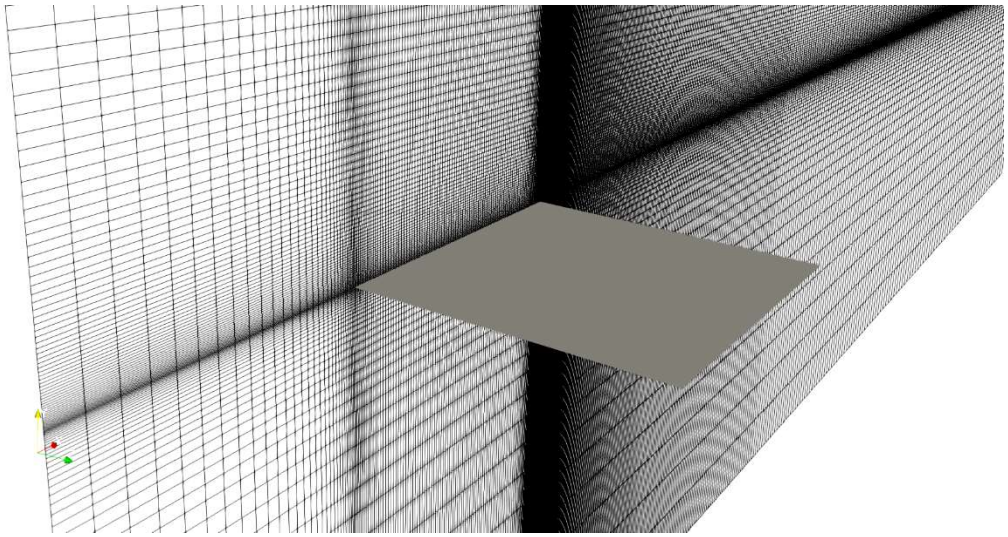

(b)

Figure 15: Close-up view of the resolution around the airfoil for (a) coarse grid and (b) fine grid

5.2 Numerical Methods

To address some of the issues related to numerical dissipation and model dependency experienced in the previous study, three dimensional simulations were performed using MILES and OGRE low-dissipation scheme in Loci-CHEM [16], a finite-volume flow solver developed at Mississippi State University that can solve chemically reacting viscous flows using density-based algorithms, implicit numerical methods, and high-resolution approximate Riemann solvers.

The initial conditions used for the simulations is shown in Figure 16.

Re_c	**AoA**	**Turbulence Intensity**	**c**	**μ**	**U_∞**	**ρ**
$4.6x10^6$	10°	1%	1.009 m	$1.794x10^{-5}$ kg/m-s	70 m/s	1.225 kg/m^3

Figure 16: Table of inlet and initial conditions for flat plate simulations

CHAPTER VI

RESULTS

Numerical simulation data for the coarse and fine grids were postprocessed using Paraview [23]. Distribution of flow and statistical variables were extracted in the spanwise and streamwise planes to identify the structure of the vortex and the its region of influence. The following sections compare the relative performance of the proposed design against the baseline airfoil designs considered in this study.

6.1 Coarse Grid Results

The following sections include postprocessed data for the coarse grid.

6.1.1 Mean and Instantaneous Velocity Magnitude Contours on Spanwise Planes

Figures 17 thru 24 show contours of mean and instantaneous velocity on spanwise planes at 80%, 90%, 100%, and 105% span for each airfoil configuration. As the flow approaches the leading edge, it slows down around the stagnation region at the base of the leading edge on the pressure side. On the suction side, flow accelerates over the leading edge followed by a separation bubble shown at 80% and 90% span. Although these particular characteristics do not vary from one airfoil design to another, the effect of winglets and slits alter the separation bubble to a certain extent. Both the winglet variants show a larger leading-edge separation bubble than their baseline variants, while the slits introduce trailing edge separation.

Figures also indicate that the baseline configuration contains a region of influence between 90% and 105% span where majority of the velocity fluctuations occur. All other designs exhibit a region of diffused vortex core with relatively lower velocities. The introduction of winglets and

slits introduces the formation of turbulent fluctuations aft of the airfoil which help in diffusing some of the momentum and energy of the wingtip vortex.

(a)

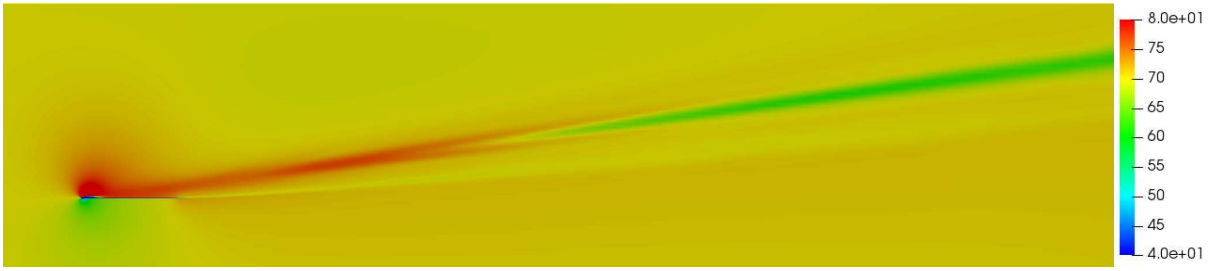

(b)

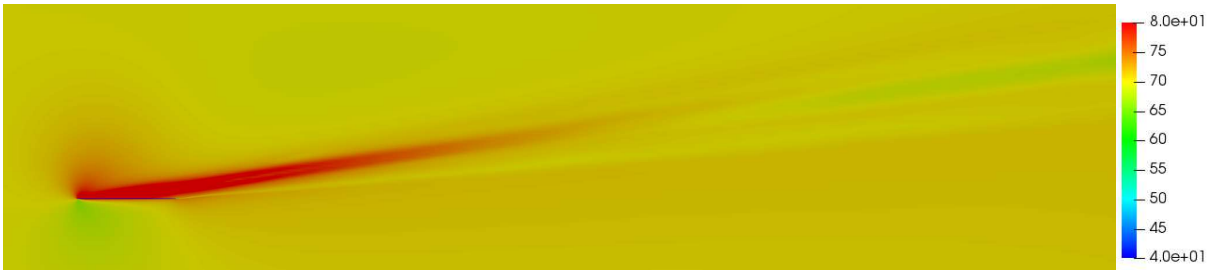

(c)

(d)

Figure 17: Contours of mean-velocity magnitude for the coarse grid at (a) 80% span, (b) 90% span, (c) 100% span, and (d) 105% span for a flat plate

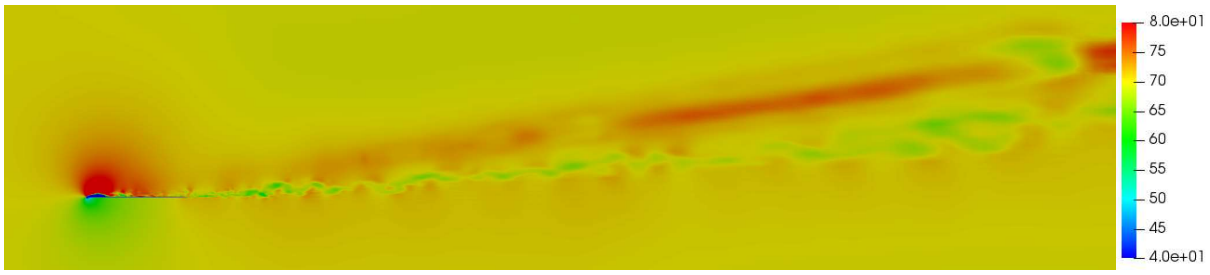

(a)

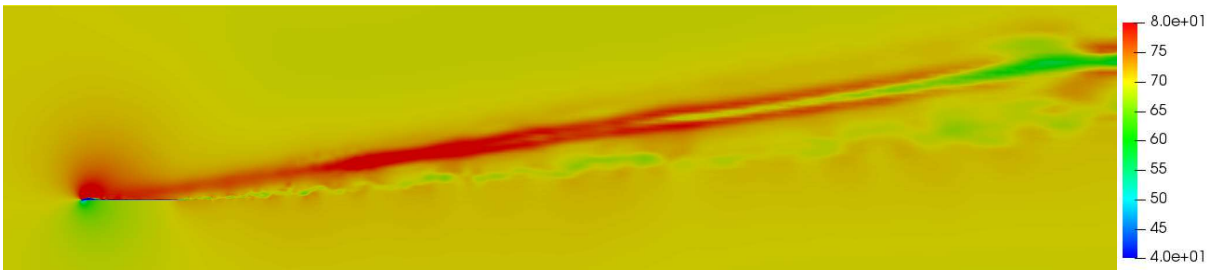

(b)

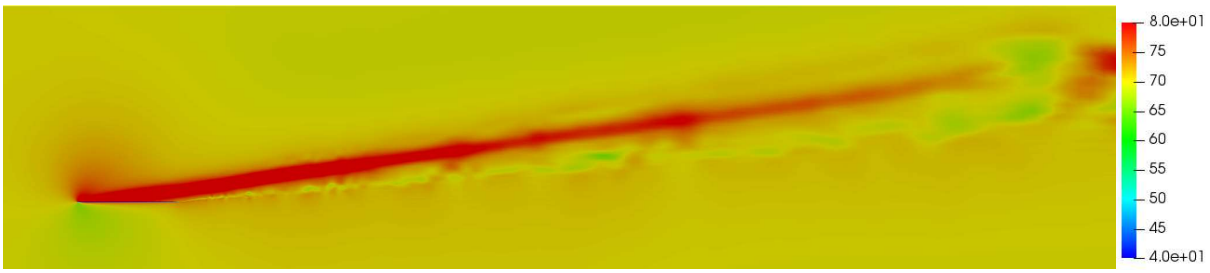

(c)

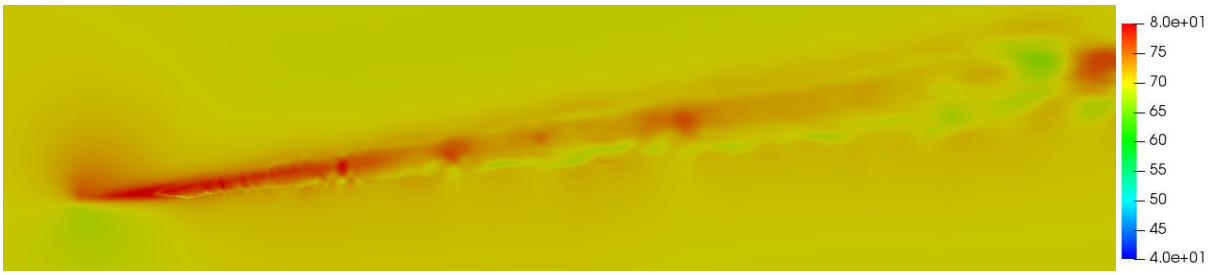

(d)

Figure 18: Contours of instantaneous-velocity magnitude for the coarse grid at (a) 80% span, (b) 90% span, (c) 100% span, and (d) 105% span for a flat plate

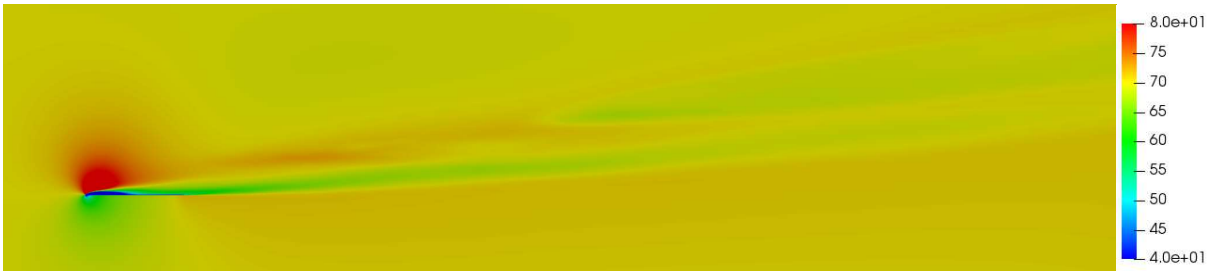

(a)

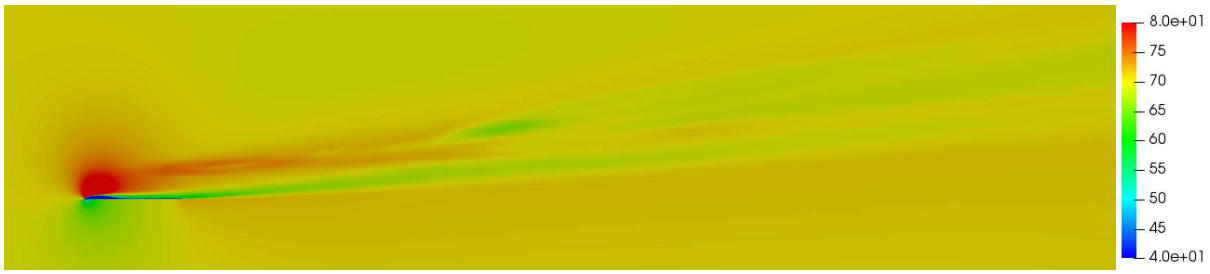

(b)

(c)

(d)

Figure 19: Contours of mean-velocity magnitude for the coarse grid at (a) 80% span, (b) 90% span, (c) 100% span, and (d) 105% span for a flat plate with winglet

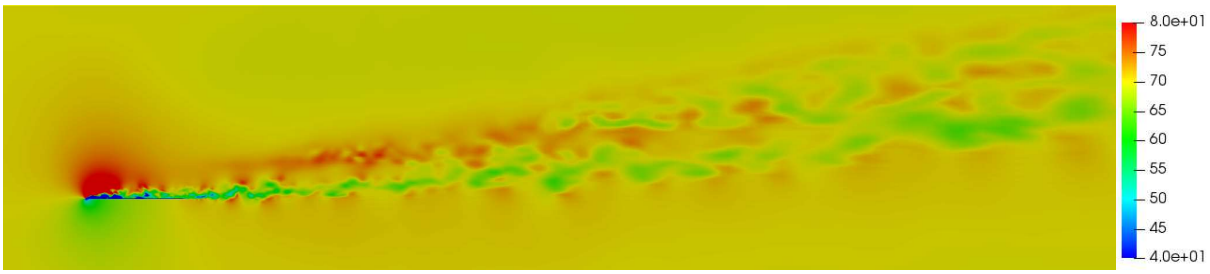
8.0e+01
75
70
65
60
55
50
45
4.0e+01

(a)

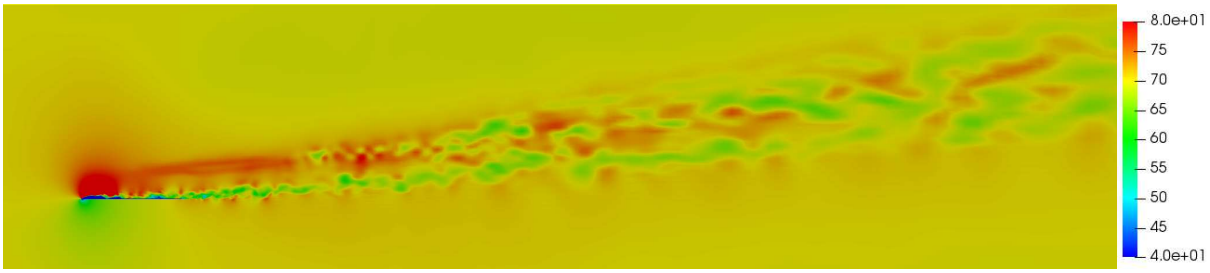
8.0e+01
75
70
65
60
55
50
45
4.0e+01

(b)

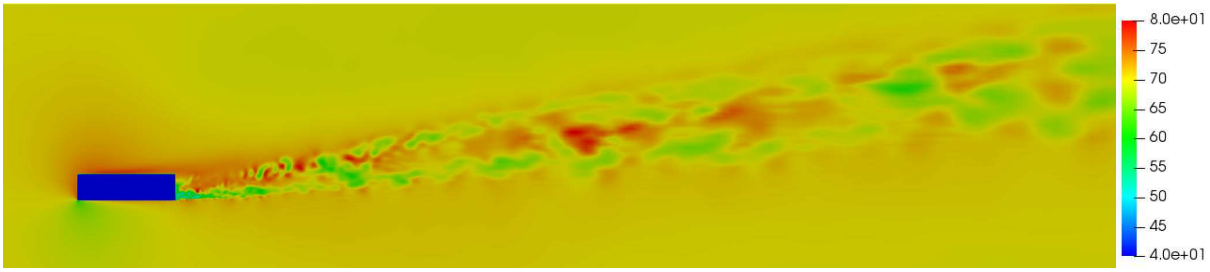
8.0e+01
75
70
65
60
55
50
45
4.0e+01

(c)

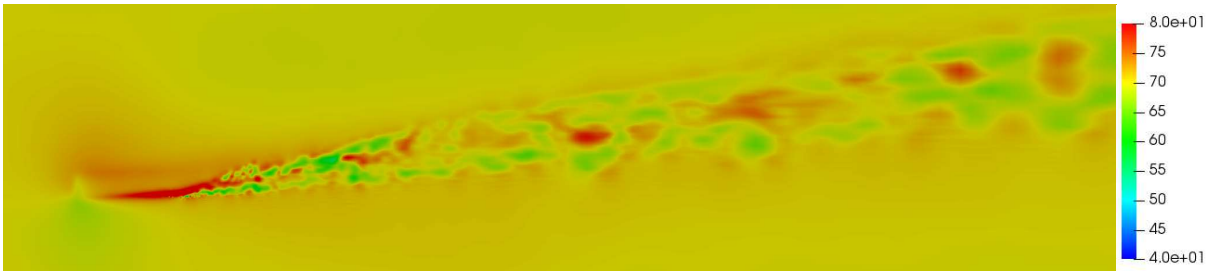

(d)

Figure 20: Contours of instantaneous-velocity magnitude for the coarse grid at (a) 80% span, (b) 90% span, (c) 100% span, and (d) 105% span for a flat plate with winglet

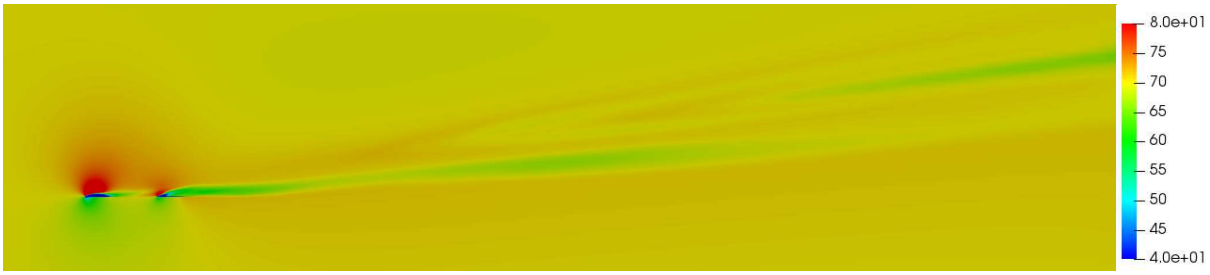

(a)

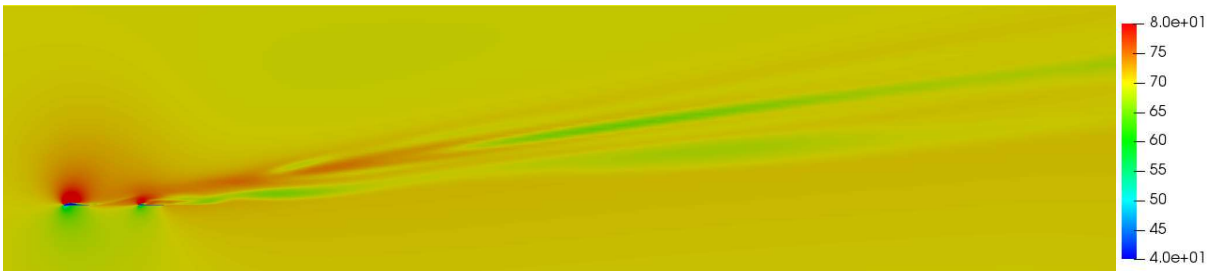

(b)

(c)

(d)

Figure 21: Contours of mean-velocity magnitude for the coarse grid at (a) 80% span, (b) 90% span, (c) 100% span, and (d) 105% span for a flat plate with slits

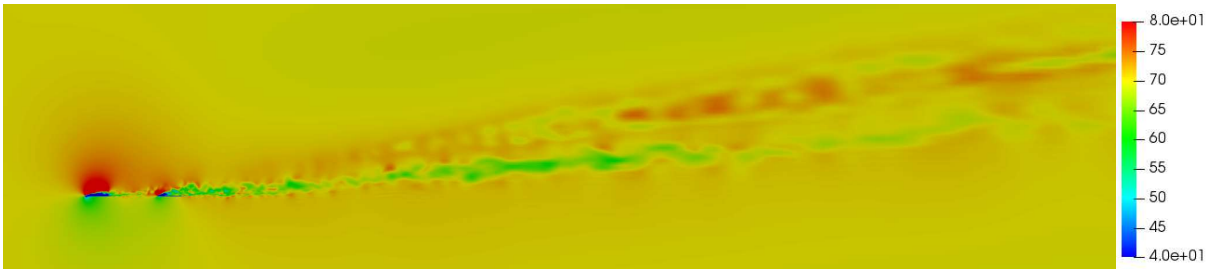

(a)

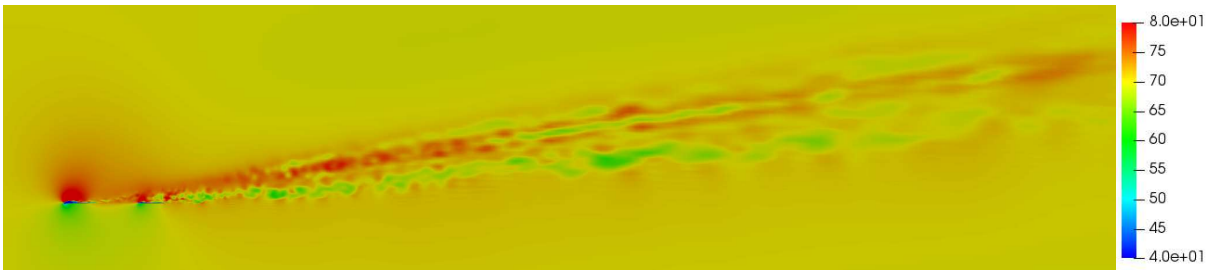

(b)

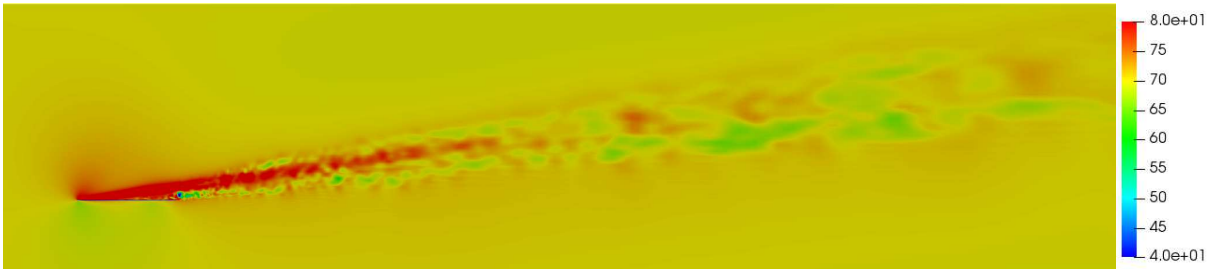

(c)

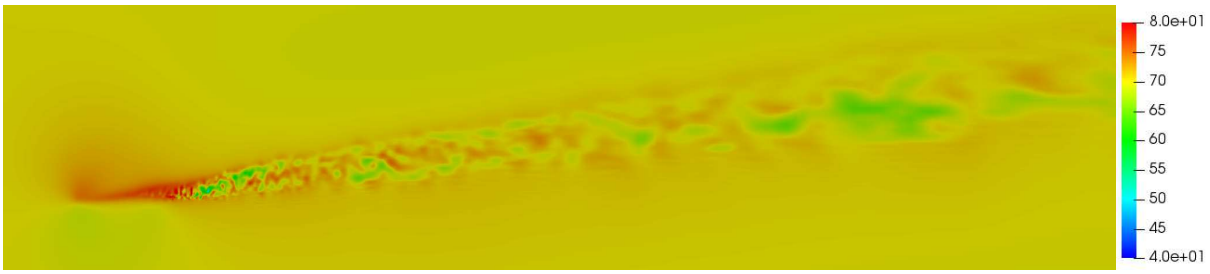

(d)

Figure 22: Contours of instantaneous-velocity magnitude for the coarse grid at (a) 80% span, (b) 90% span, (c) 100% span, and (d) 105% span for a flat plate with slits

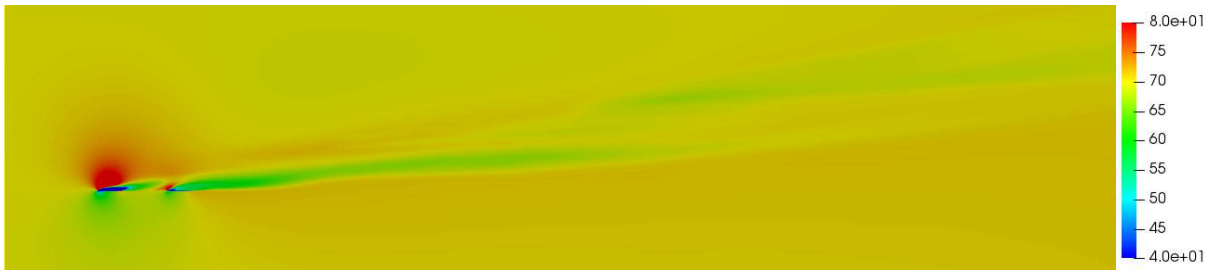
8.0e+01
75
70
65
60
55
50
45
4.0e+01

(a)


8.0e+01
75
70
65
60
55
50
45
4.0e+01

(b)


8.0e+01
75
70
65
60
55
50
45
4.0e+01

(c)

(d)

Figure 23: Contours of mean-velocity magnitude for the coarse grid at (a) 80% span, (b) 90% span, (c) 100% span, and (d) 105% span for a flat plate with slits and winglet

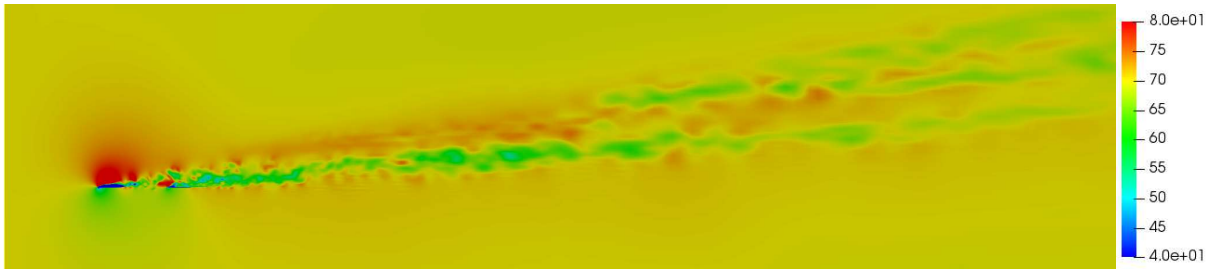

(a)

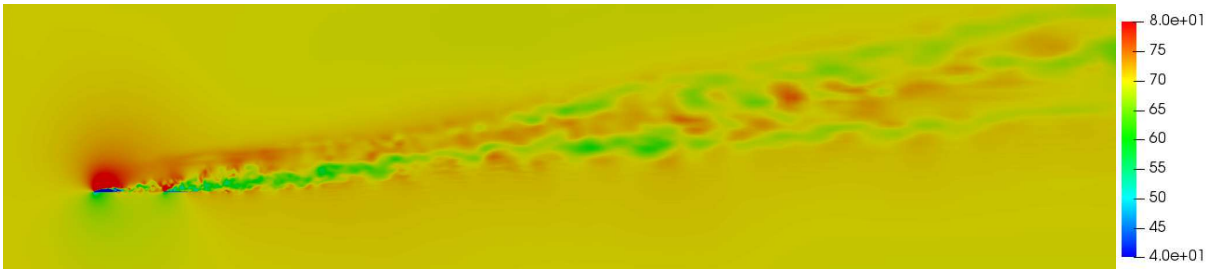

(b)

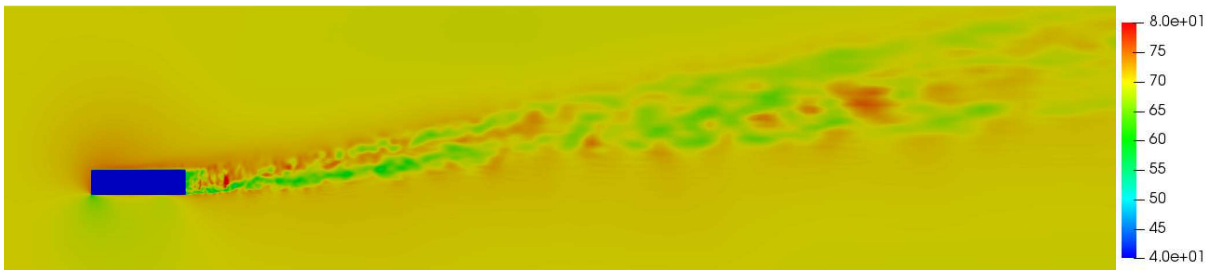

(c)

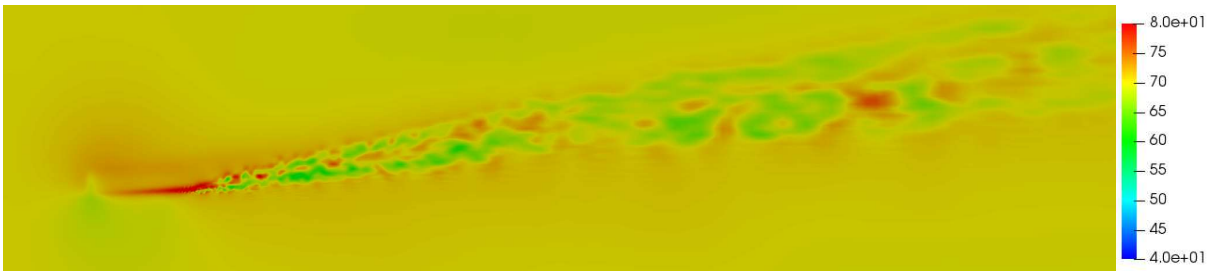

(d)

Figure 24: Contours of instantaneous-velocity magnitude for the coarse grid at (a) 80% span, (b) 90% span, (c) 100% span, and (d) 105% span for a flat plate with slits and winglet

6.1.2 Mean-Vorticity Magnitude Contours on Spanwise Planes

To accurately investigate the performance of the proposed design in mitigating wingtip vortices, analysis of the vortex strength is imperative. Vorticity describes the local spinning motion of the continuum; a region of lower vorticity would imply a weakened vortex while a region of higher vorticity would imply a stronger vortex. Equations 20 and 21 describe vorticity and vorticity magnitude respectively.

$$\overline{\omega_{ij}} = \left(\frac{\partial \bar{U}_i}{\partial x_j} - \frac{\partial \bar{U}_j}{\partial x_i}\right) \tag{20}$$

$$\left\|\overline{\omega_{ij}}\right\| = \sqrt{\left(2\overline{\omega_{ij}}\,\overline{\omega_{ij}}\right)} \tag{21}$$

Figures 25 thru to 28 show the streamwise distribution of vorticity magnitude at 80%, 90%, 100%, and 105% spans. The vorticity magnitude contours confirm that the wingtip vortex formed by the flat plate is confined tightly within a small region between 90% and 105% span. All the airfoil configurations show maximum vorticity between 2c and 6c behind the airfoil at 90% span, and up to 2c behind the airfoil at 100% span indicating some spanwise movement of the vortex core. Surprisingly, the introduction of the slits into the baseline flat plat does not show any significant reduction of vorticity magnitude at 90% span. The winglet configurations however, show reduced vortex strength and the formation of smaller regions of vorticity regions throughout the spanwise planes. This vortex disruption can be attributed to the formation of multiple smaller vortices as suggested by figures 26 and 27 which interact with wingtip vortex. Overall, the proposed design seems to alter the behavior of the wingtip vortex for both the designs considered in this study. The increased vorticity for the flat plat with slits is a numerical artifact that will be addressed in the following sections.

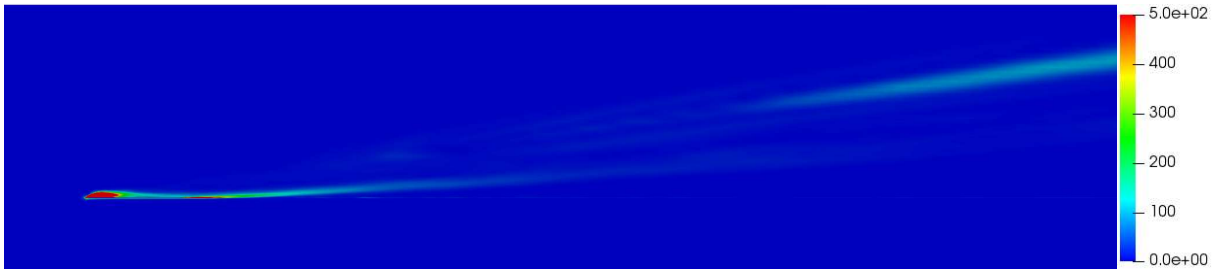

(a)

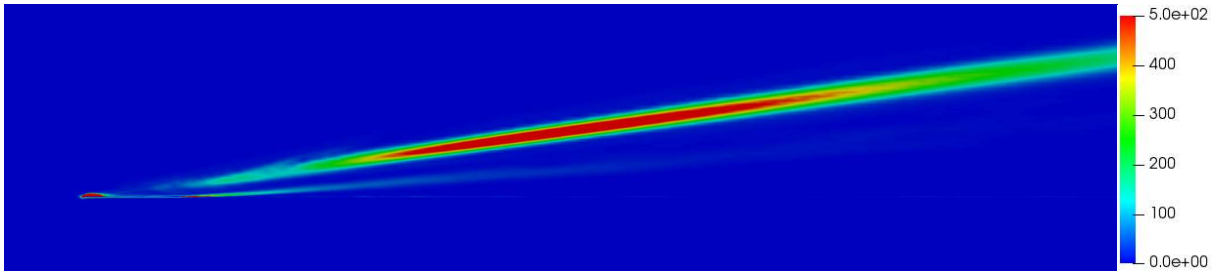

(b)

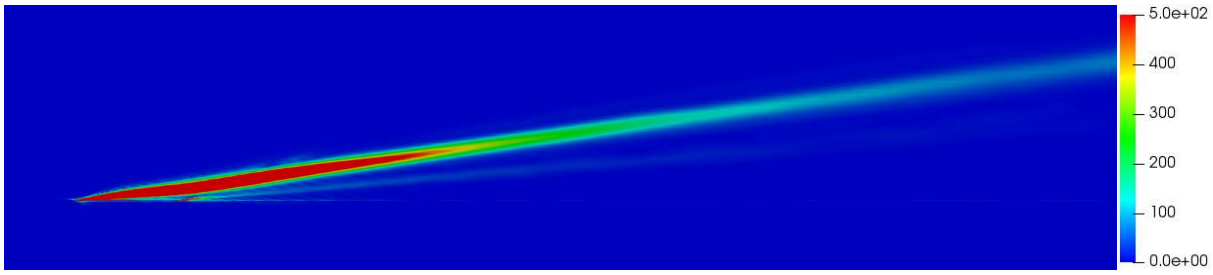

(c)

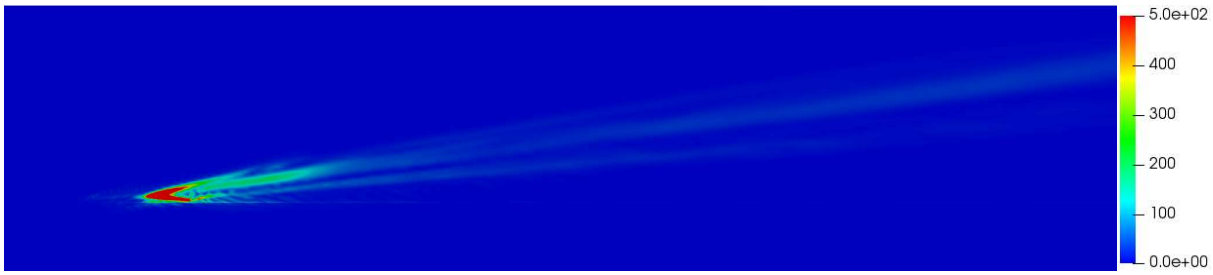

(d)

Figure 25: Contours of mean-vorticity magnitude for the coarse grid at (a) 80% span, (b) 90% span, (c) 100% span, and (d) 105% span for a flat plate

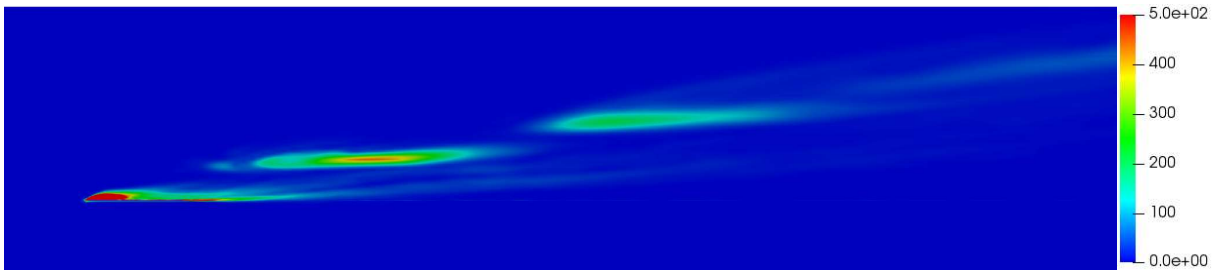
5.0e+02
400
300
200
100
0.0e+00

(a)

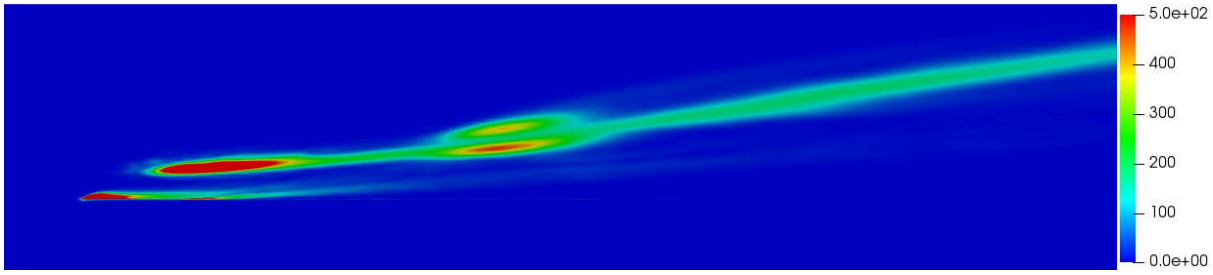
5.0e+02
400
300
200
100
0.0e+00

(b)

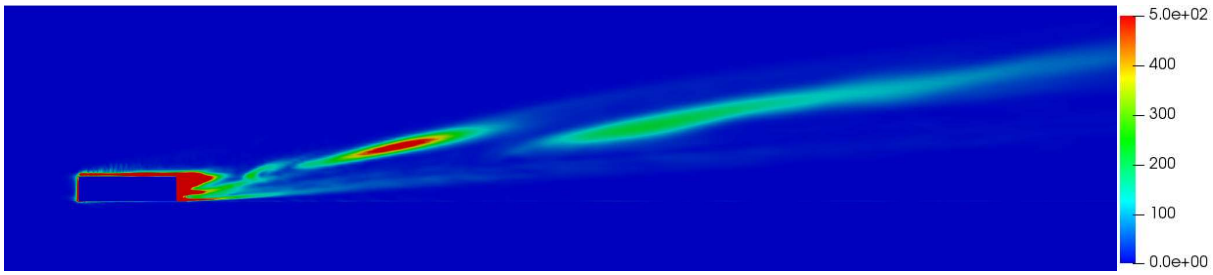
5.0e+02
400
300
200
100
0.0e+00

(c)

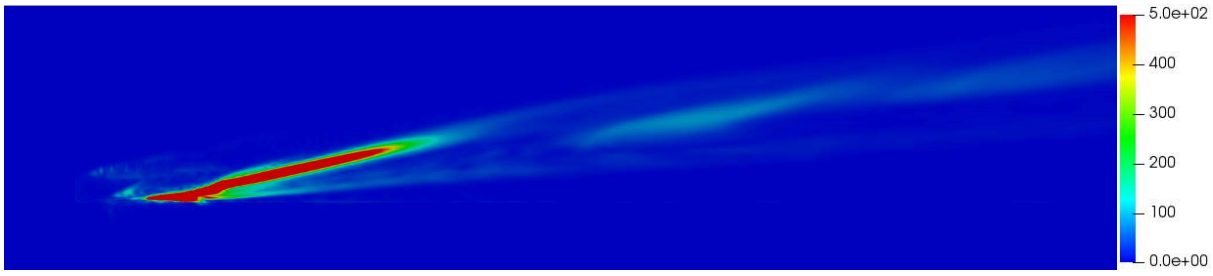

(d)

Figure 26: Contours of mean-vorticity magnitude for the coarse grid at (a) 80% span, (b) 90% span, (c) 100% span, and (d) 105% span for a flat plate winglet

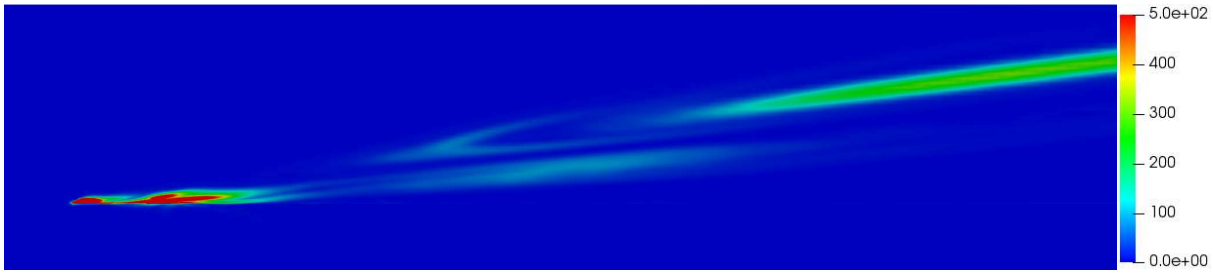

(a)

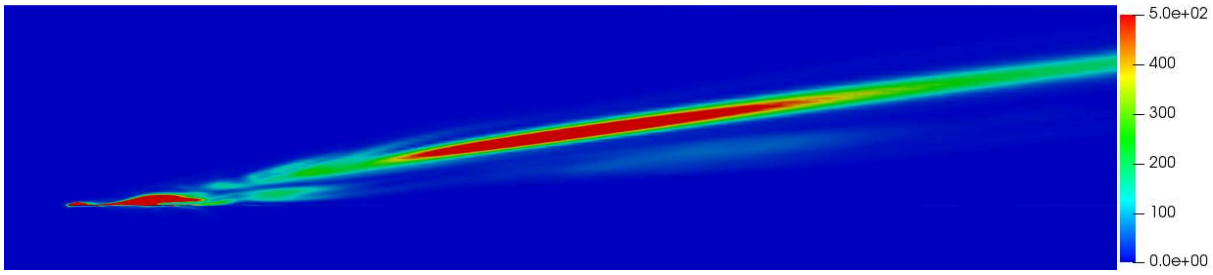

(b)

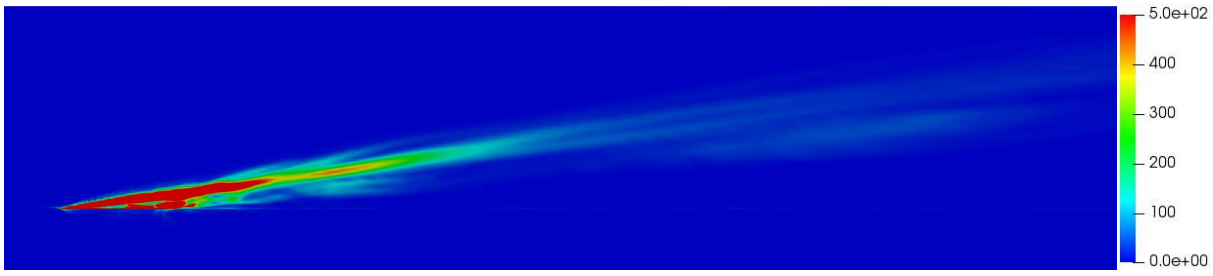

(c)

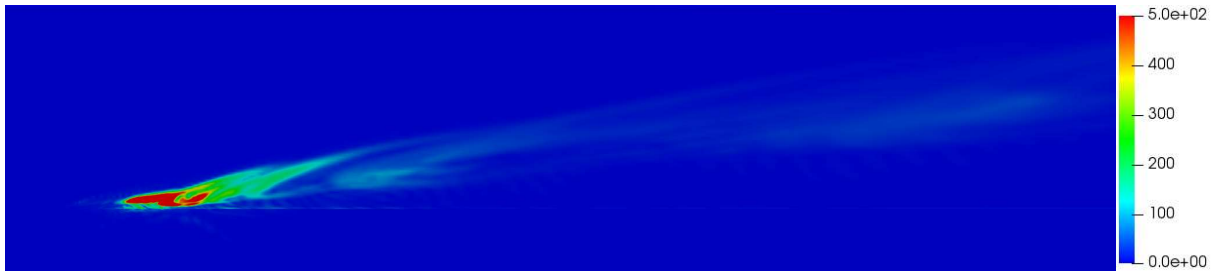

(d)

Figure 27: Contours of mean-vorticity magnitude for the coarse grid at (a) 80% span, (b) 90% span, (c) 100% span, and (d) 105% span for a flat plate with slits

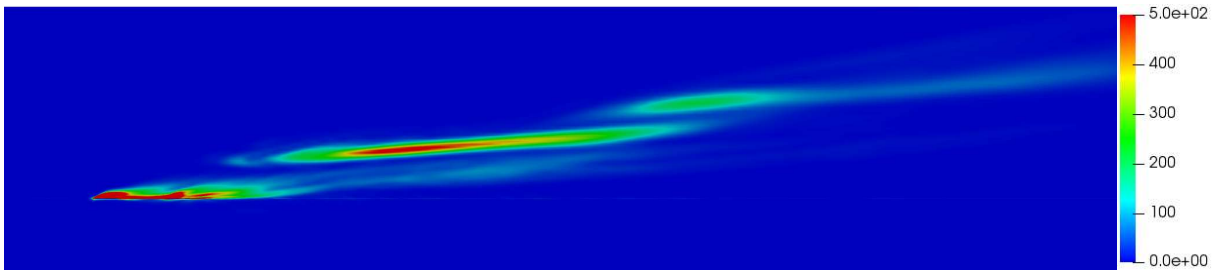

(a)

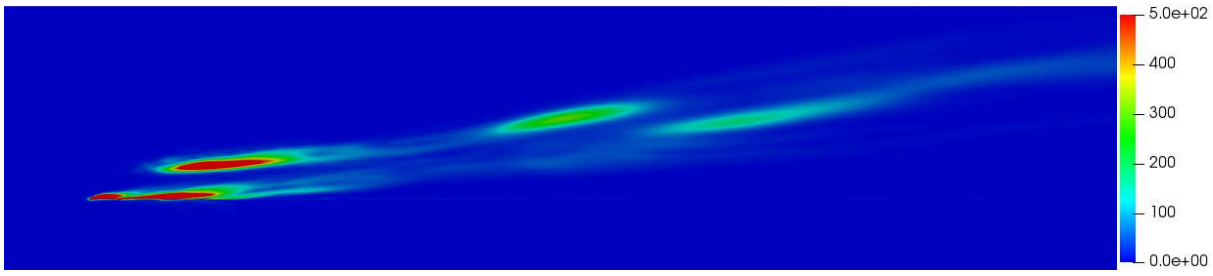

(b)

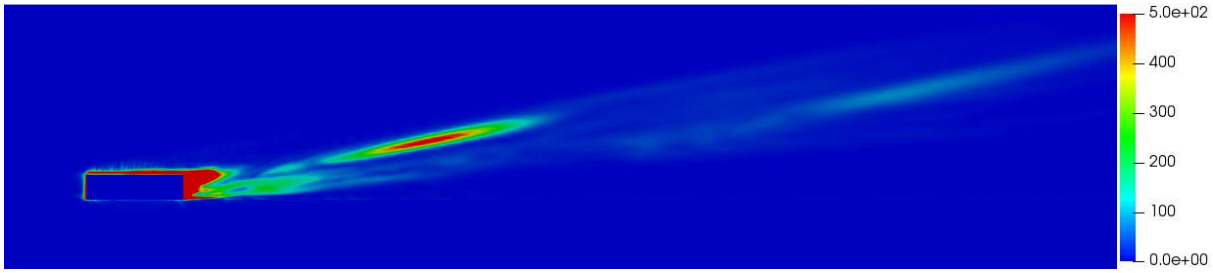

(c)

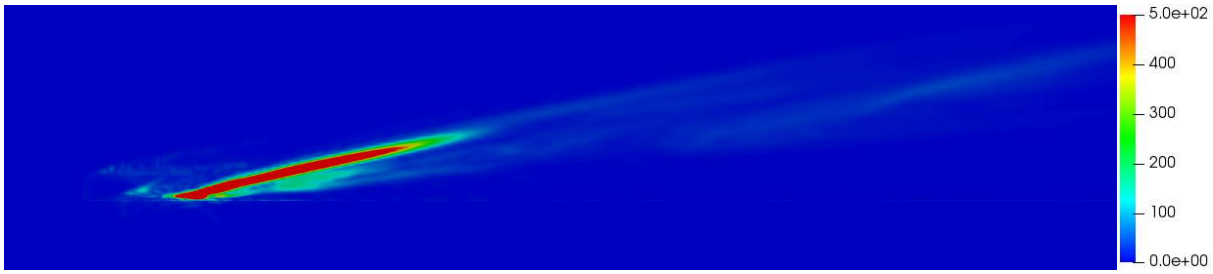

(d)

Figure 28: Contours of mean-vorticity magnitude at for the coarse grid (a) 80% span, (b) 90% span, (c) 100% span, and (d) 105% span for a flat plate with slits and winglet

6.1.3 Mean-Vorticity Magnitude Contours on Streamwise Planes

Figures 29 thru 32 compare the generation and the development of wingtip vortices on streamwise planes. For the flat plate, a single coherent vortex formation is observed with some vorticity generated on the suction side of the airfoil. The introduction of a winglet causes the

formation of two vortices, a primary vortex from the tip of the winglet and a secondary vortex from the winglet attachment junction. These two vortices interact and merge to form a weaker vortex at 8c (7c aft of the airfoil). For both the modified designs, significant turbulence is generated by the presence of the slits and several smaller vortices are observed. Surprisingly, the vortices do not help diffuse the primary wingtip vortex formed by the flat plate with slits and neither is there any observable reduction in vortex strength for this configuration. The flat plate with slits and winglet shows reduced overall vorticity compared all other design configurations caused by multiple vortices formed on the suction side which contribute to the increased diffusion compared to the other configurations.

The vorticity contours also indicate the presence of noise around the airfoil which can be attributed to the skewness of the grid caused by high-aspect ratio cells. For example, Figure 32 (c) shows a region of higher vorticity below the wingtip vortex compared to its surrounding areas. Similar numerical artifacts can be observed in the same location for all the cases which manifests itself as an increase or decrease in vorticity. The presence of noise and the increased vorticity prompted the use of a fine grid to accurately evaluate the performance of the proposed design.

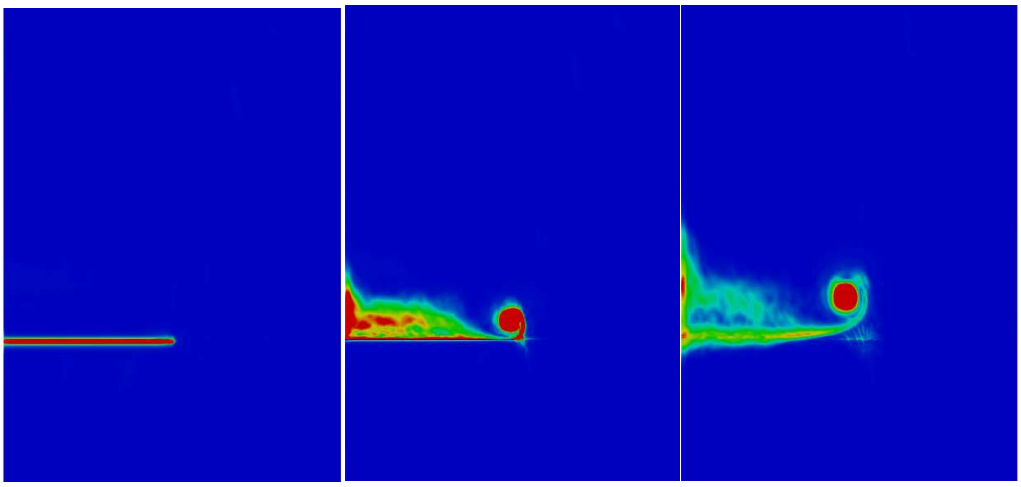

(a) (b) (c)

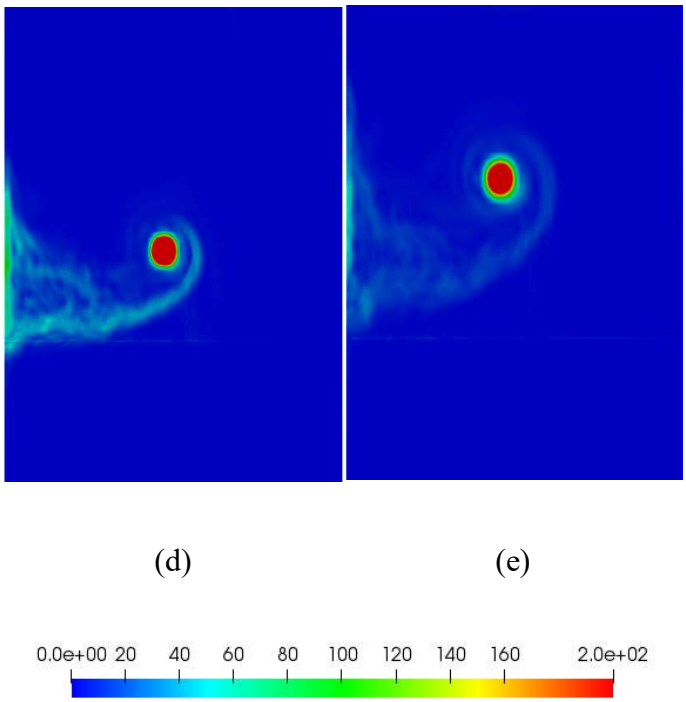

(d) (e)

Figure 29: Contours of mean-vorticity magnitude for the coarse grid at (a) 1c (leading-edge), (b) 2c, (c) 3c, (d) 5c, and (e) 8c for a flat plate

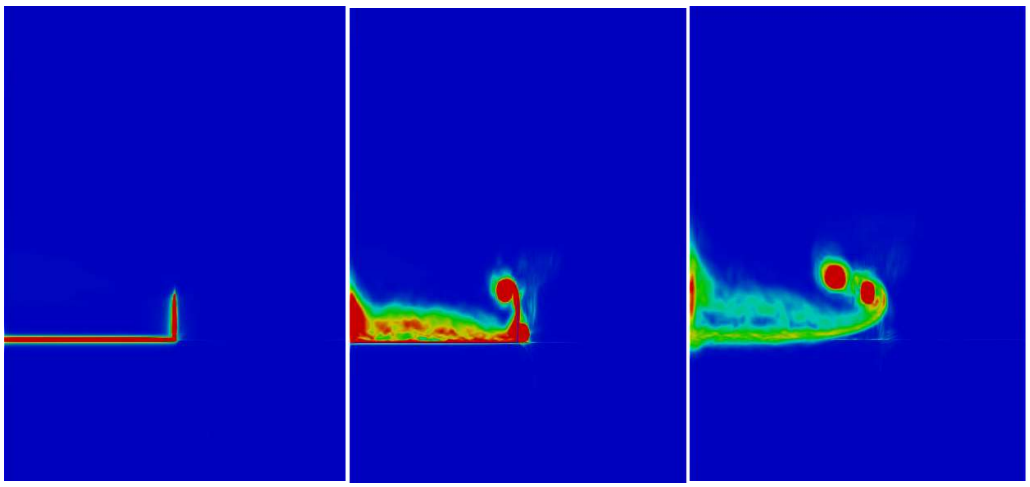

(a) (b) (c)

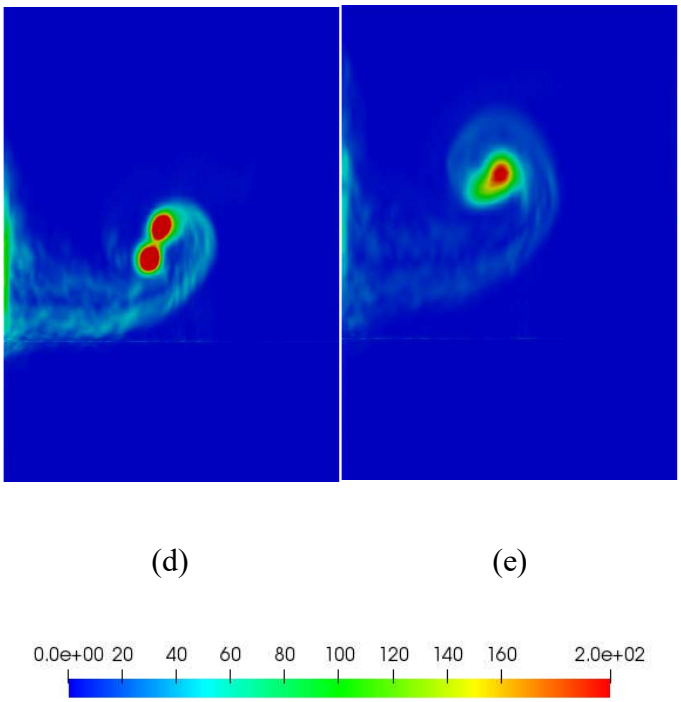

(d) (e)

Figure 30: Contours of mean-vorticity magnitude for the coarse grid at (a) 1c (leading-edge), (b) 2c, (c) 3c, (d) 5c, and (e) 8c for a flat plate with winglet

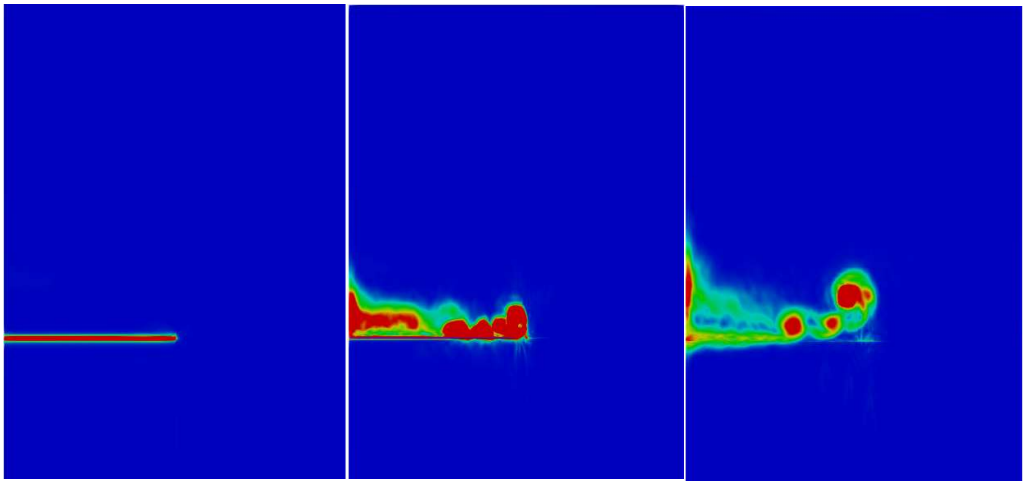

(a) (b) (c)

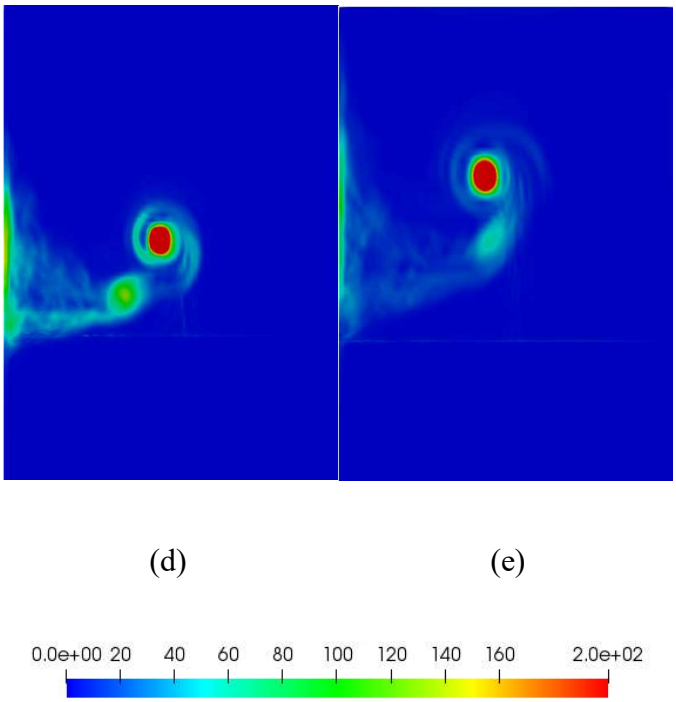

(d) (e)

Figure 31: Contours of mean-vorticity magnitude for the coarse grid at (a) 1c (leading-edge), (b) 2c, (c) 3c, (d) 5c, and (e) 8c for a flat plate with slits

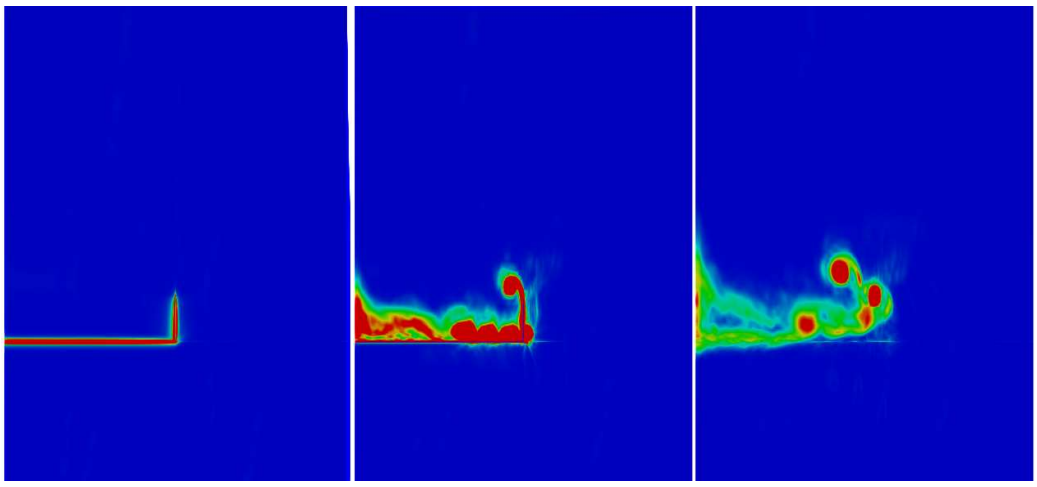

(a) (b) (c)

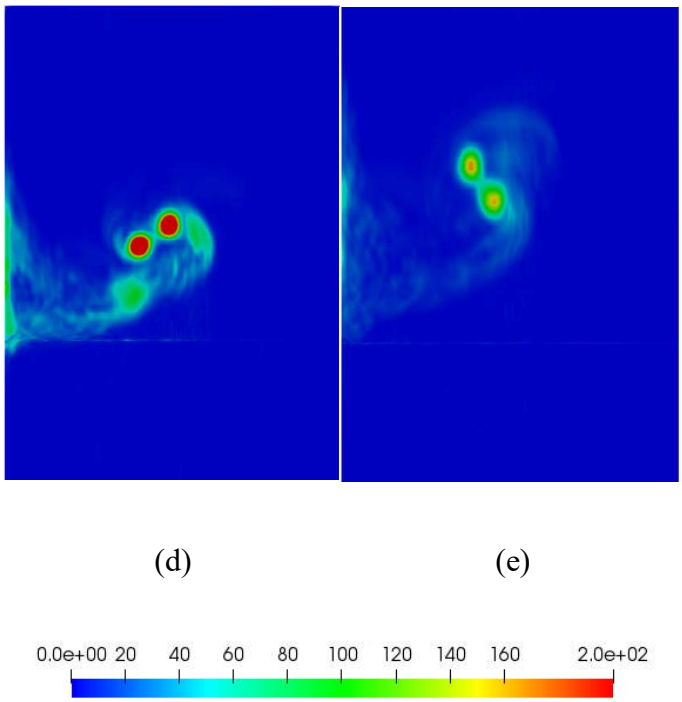

Figure 32: Contours of mean-vorticity magnitude for the coarse grid at (a) 1c (leading-edge), (b) 2c, (c) 3c, (d) 5c, and (e) 8c for a flat plate with slits and winglet

6.2 Fine Grid Results

The following sections include postprocessed data for the fine grid. Since fine grid mean and instantaneous-velocity magnitude contours were almost identical to the coarse grid except for a better resolution of the smaller scales, they have been omitted from this section.

6.2.1 Mean-Vorticity Magnitude Contours on Spanwise Planes

The fine grid mean-vorticity magnitude contours show a significant reduction of vorticity for the airfoil configurations using the slits. The regions of high vorticity seem to decay faster than the coarse grid. This can be attributed to the introduction of small-scale fluctuations that aids in the vortex diffusion process. Also, with improved skewness and higher cell density, the flat plate with slits in Figure 33 shows a significantly reduced vorticity for the flat plate with slits at 90%.

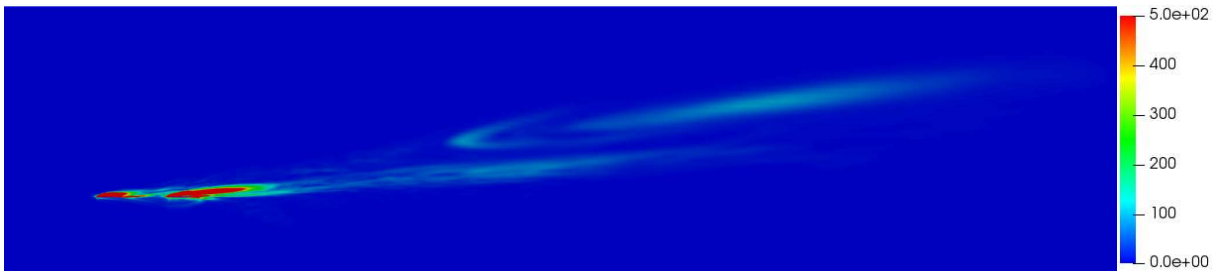
5.0e+02
400
300
200
100
0.0e+00

(a)

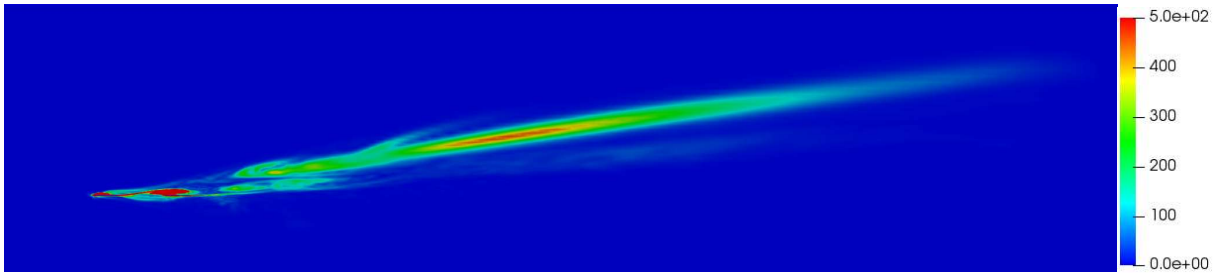
5.0e+02
400
300
200
100
0.0e+00

(b)

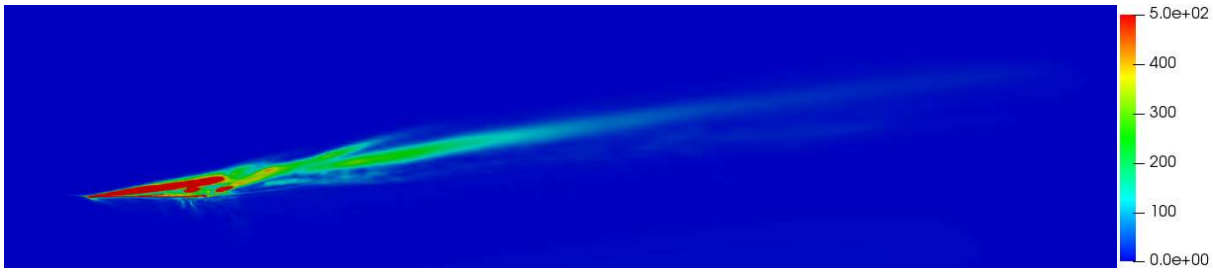
5.0e+02
400
300
200
100
0.0e+00

(c)

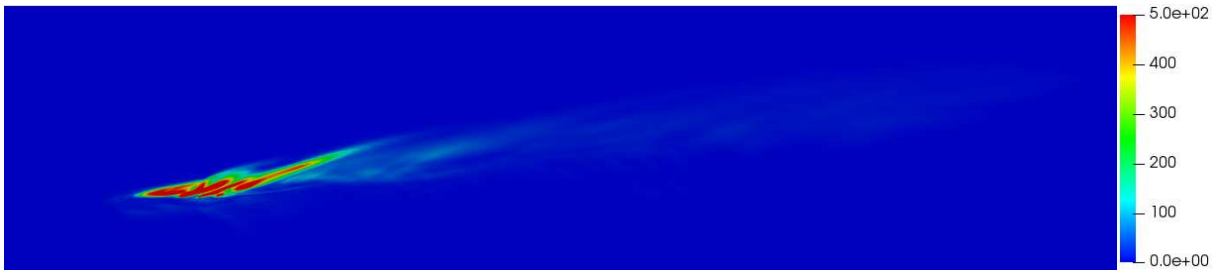

(d)

Figure 33: Contours of mean-vorticity magnitude for the fine grid at (a) 80% span, (b) 90% span, (c) 100% span, and (d) 105% span for a flat plate with slits

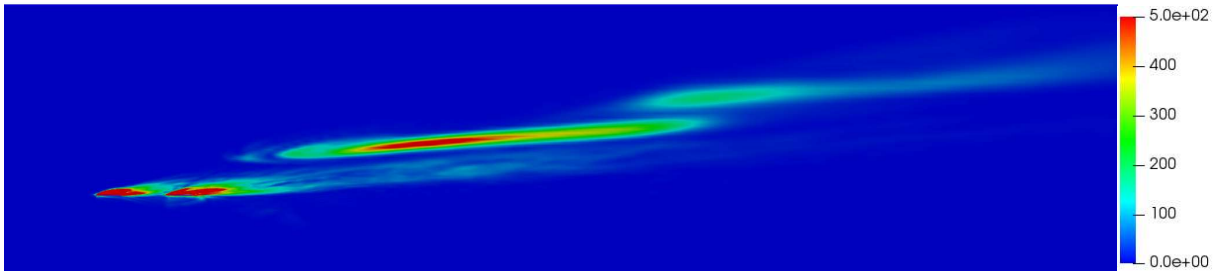

(a)

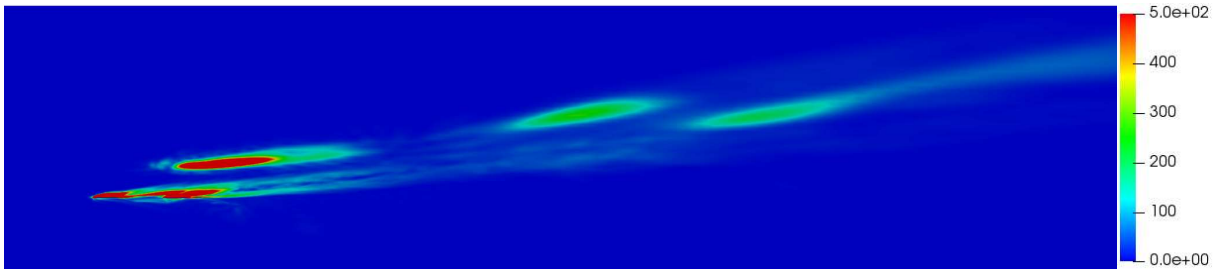

(b)

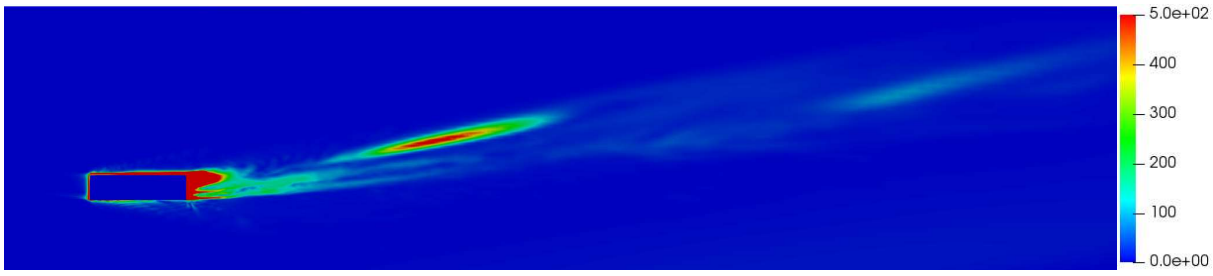

(c)

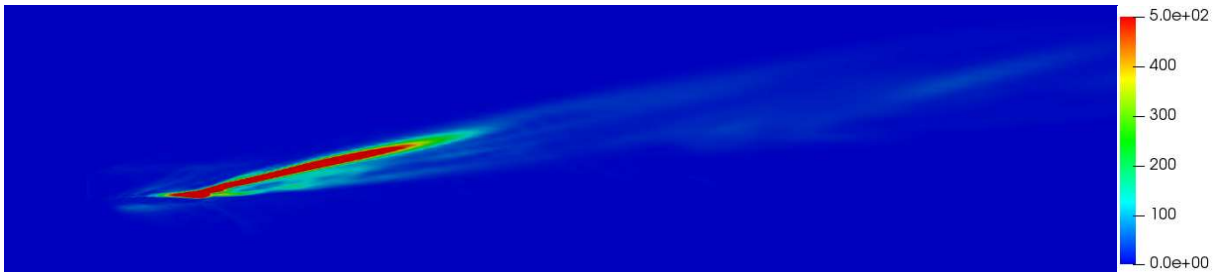

(d)

Figure 34: Contours of mean-vorticity magnitude for the fine grid at (a) 80% span, (b) 90% span, (c) 100% span, and (d) 105% span for a flat plate with slits and winglet

6.2.2 Mean-Vorticity Magnitude Contours on Streamwise Planes

The contours of mean-vorticity magnitude on streamwise planes show some differences when compared to the coarse grid results. Firstly, the numerical artifacts reported for the coarse grid under the primary vortex have somewhat disappeared. Secondly, there is a significant reduction of vortex strength for the flat plate with slits at 8c which can be attributed to the reduction of noise caused by higher grid resolution at that location and the introduction of smaller scales of motion which aid in vorticity diffusion. Overall, both the proposed design variants now show a significant reduction in vortex strength as opposed to their unmodified counterparts.

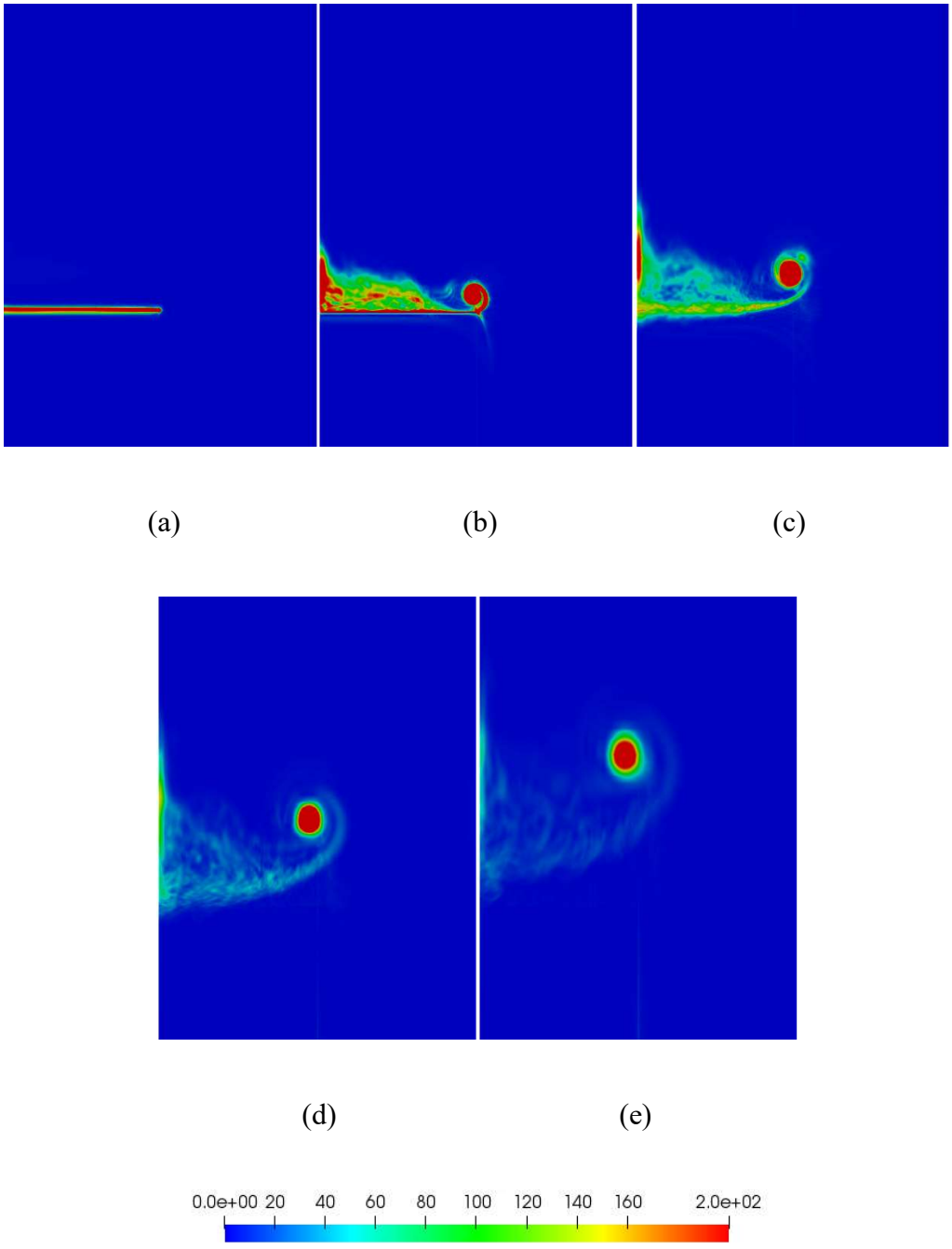

Figure 35: Contours of mean-vorticity magnitude for the fine grid at (a) 1c (leading-edge), (b) 2c, (c) 3c, (d) 5c, and (e) 8c for a flat plate

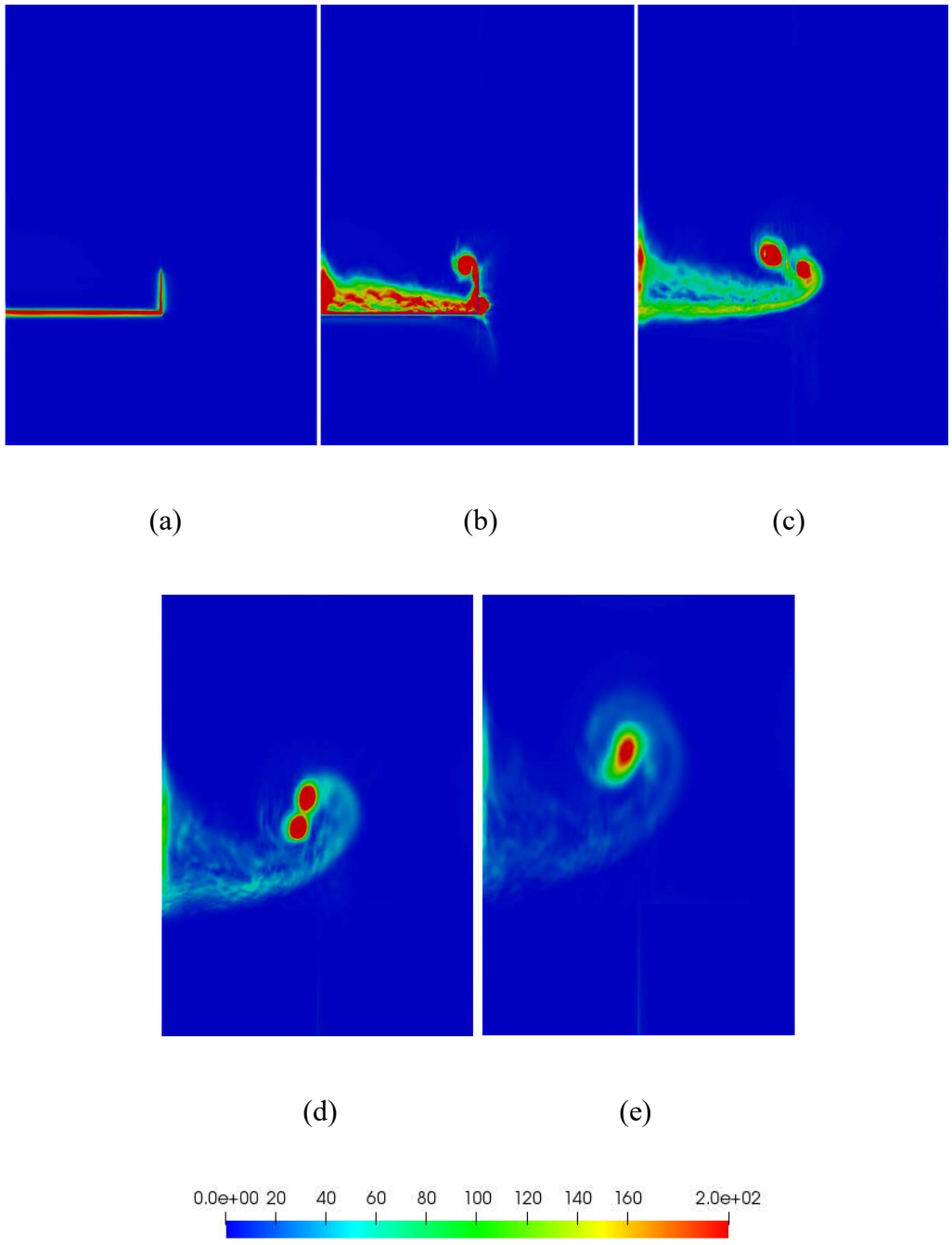

Figure 36: Contours of mean-vorticity magnitude for the fine grid at (a) 1c (leading-edge), (b) 2c, (c) 3c, (d) 5c, and (e) 8c for a flat plate with winglet

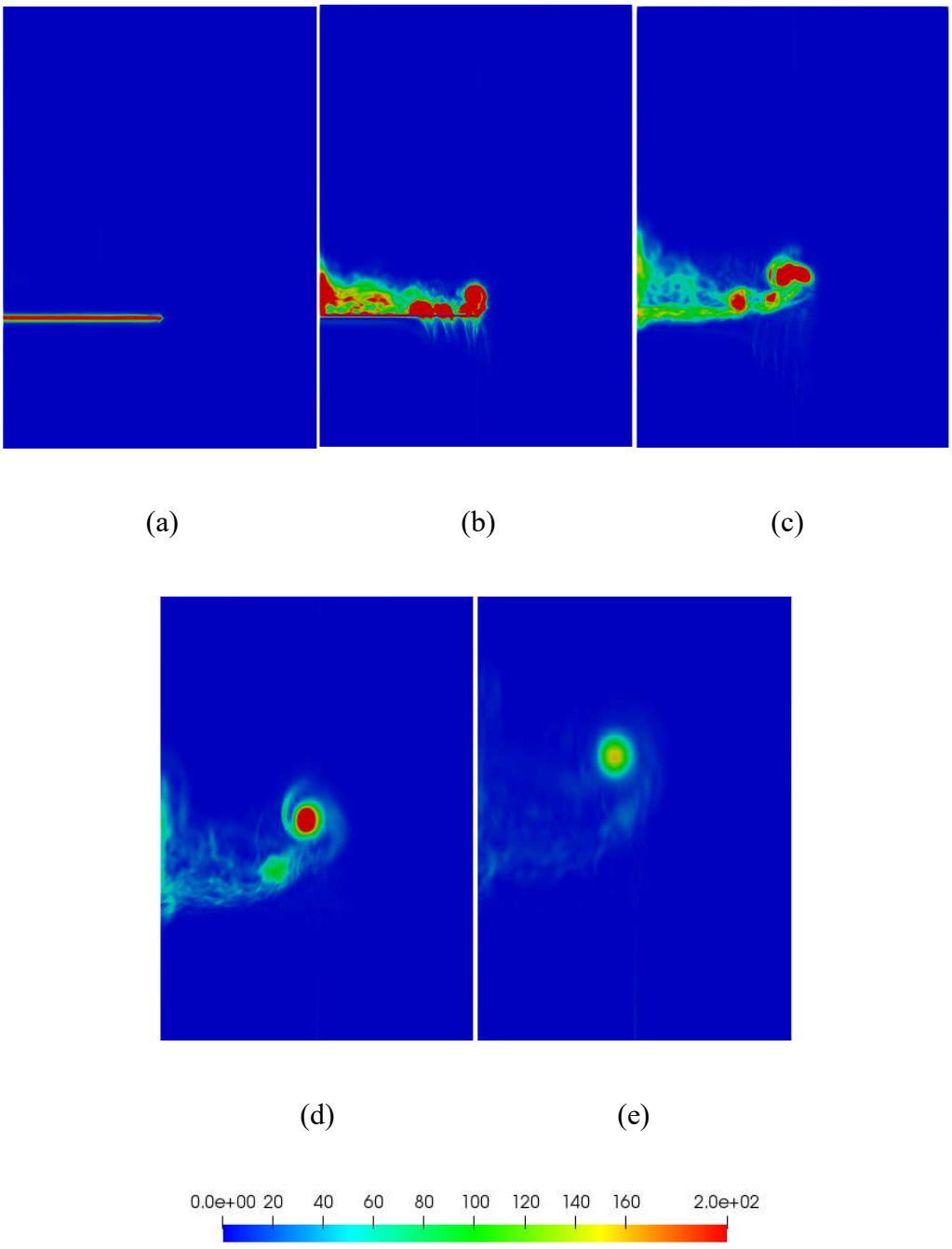

Figure 37: Contours of mean-vorticity magnitude for the fine grid at (a) 1c (leading-edge), (b) 2c, (c) 3c, (d) 5c, and (e) 8c for a flat plate with slits

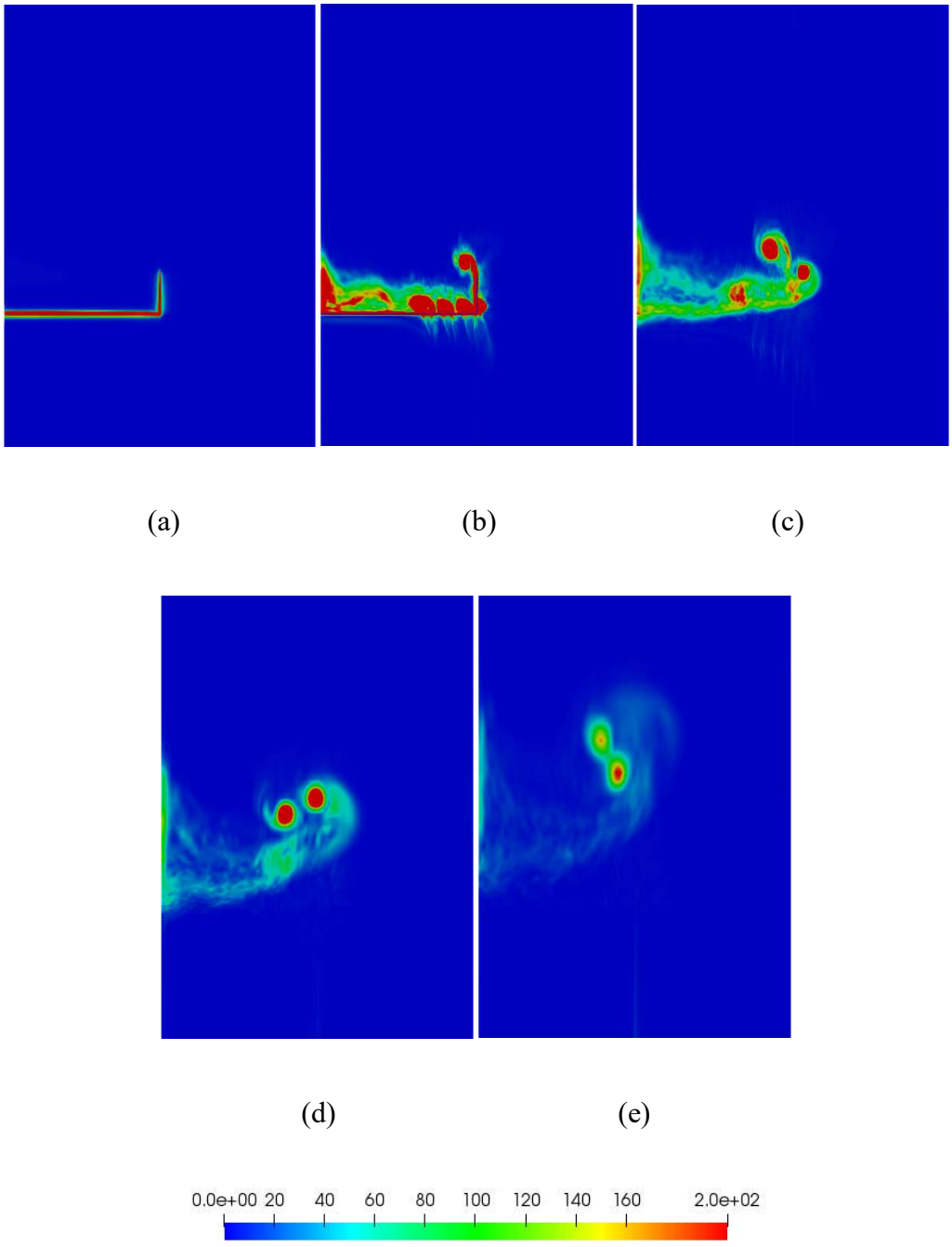

Figure 38: Contours of mean-vorticity magnitude for the fine grid at (a) 1c (leading-edge), (b) 2c, (c) 3c, (d) 5c, and (e) 8c for a flat plate with slits and winglet

6.2.3 Analysis of the Vortex Generation Mechanism

Vorticity magnitude contours on spanwise planes suggested that the introduction of slits reduced vortex strength to a certain extent. In order to better analyze the performance of the proposed design, the mechanism of vortex generation must be better understood. Figures 39 thru 45 detail the location and development of the wingtip vortices all the designs considered in this study.

For the flat plate, the initial roll up starts at 0.02c from the leading edge and remains very close to the airfoil before separating from the surface around 0.2c. Similar behavior is observed for the all the designs except for the formation of an additional vortex for the winglet configurations at the winglet tip between 0.05c and 0.2c. Both the slit configurations show the development of multiple smaller vortices from the slits. Although the flat plate with slits and winglet shows reduced vortex strength, the outer vortex remains somewhat unaffected because of the presence of the winglet. The overall reduction in vortex strength when compared to the baseline flat plate with winglet is simply due to the weakened upper vortex and its interaction with the outer vortex downstream of the airfoil. This suggests that the slit configuration for the flat plate with winglet can be potentially more effective if the outer vortex strength can be diffused.

Overall, the slit designs seem to have an impact on the growth and diffusion of the wingtip vortex but according to these results it would be more efficient make design adjustments targeting the leading edge between 0.02c-0.2c where the vortex generation mechanism is initiated. Implementation of small rakes or extrusions at the wingtips coupled with slits moved closer to the leading edge would perhaps be a more effective alternative to just the slit configuration proposed in this study.

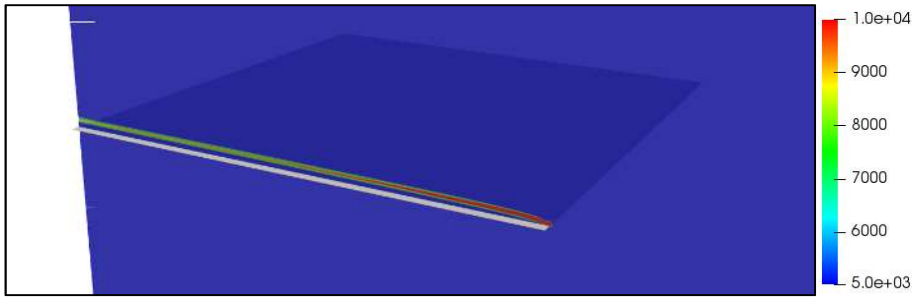

(a)

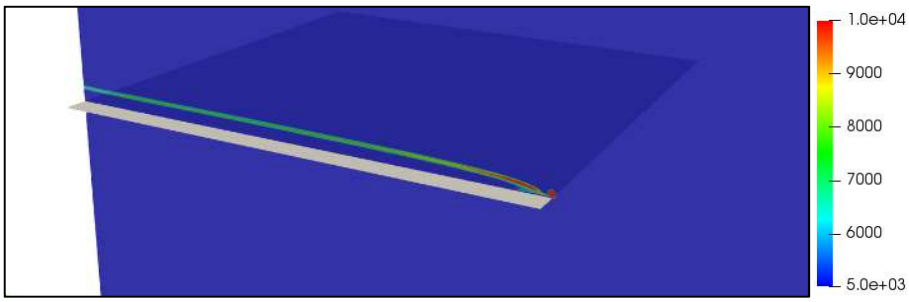

(b)

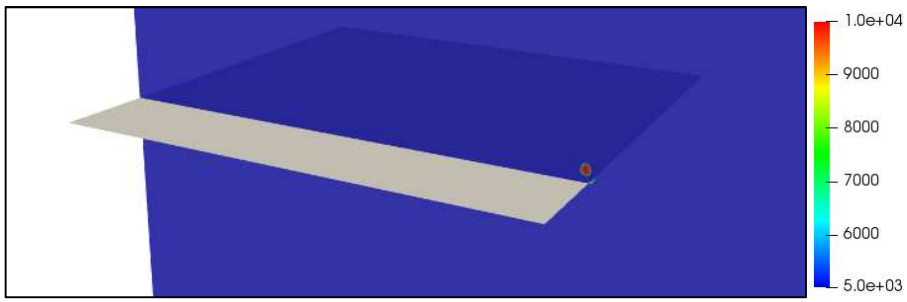

(c)

Figure 39: Contours of vorticity magnitude showing the development of the wingtip vortex for a flat plate at (a) 0.02c, (b) 0.05, and (c) 0.2c from the leading edge

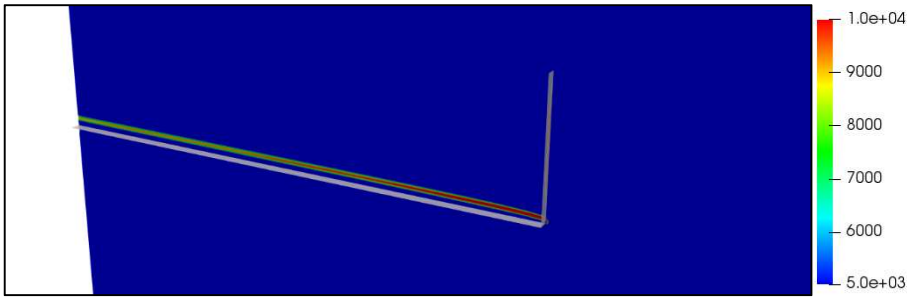

(a)

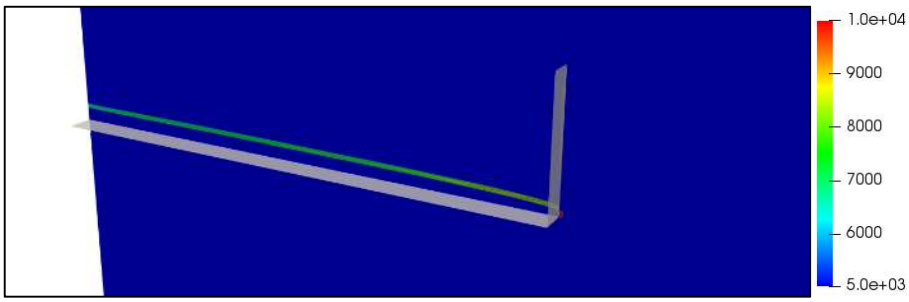

(b)

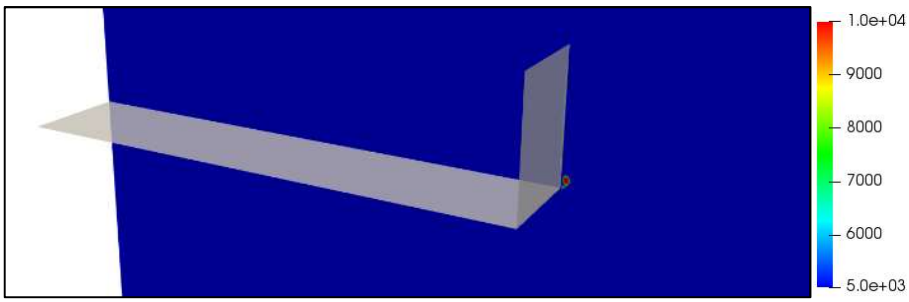

(c)

Figure 40: Contours of vorticity magnitude showing the development of primary wingtip vortex for a flat plate with winglet at (a) 0.02c, (b) 0.05, and (c) 0.2c from the leading edge

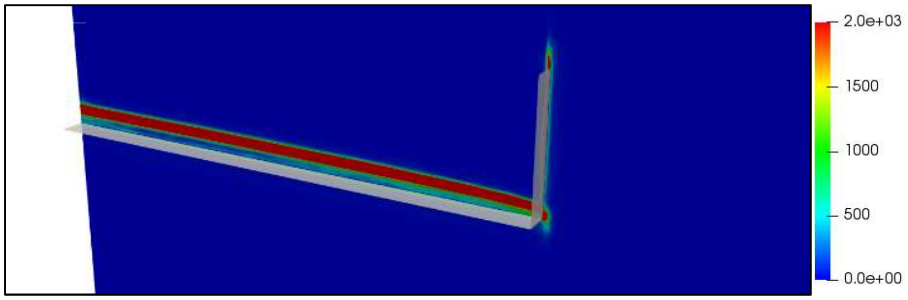

(a)

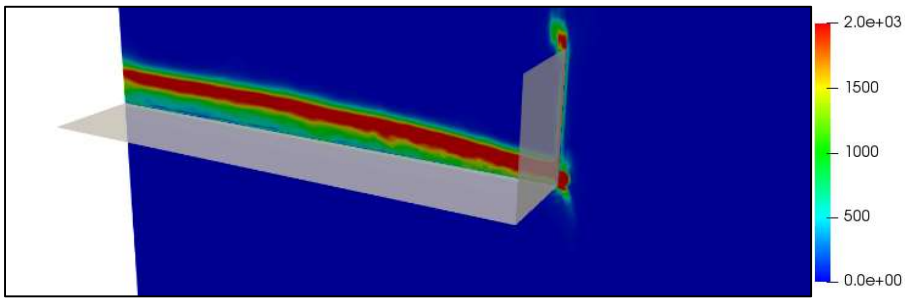

(b)

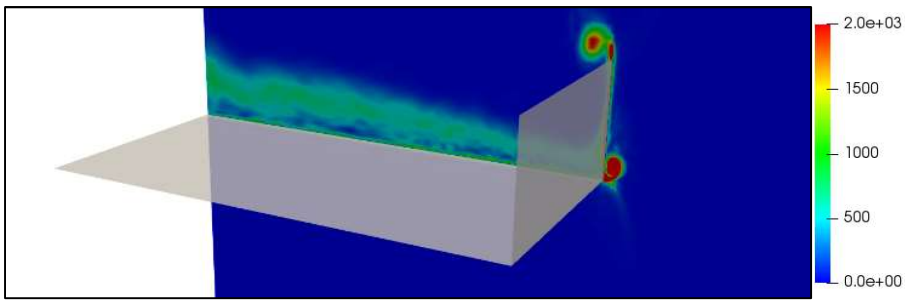

(c)

Figure 41: Contours of vorticity magnitude showing the development of secondary wingtip vortex for a flat plate with winglet for a flat plate at (a) 0.05c, (b) 0.2, and (c) 0.5c from the leading edge

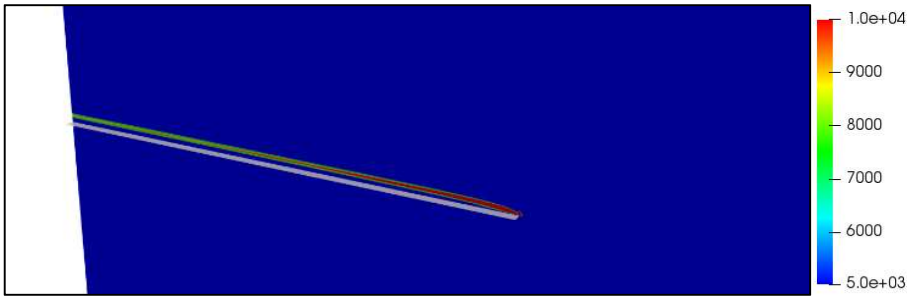
1.0e+04
9000
8000
7000
6000
5.0e+03

(a)

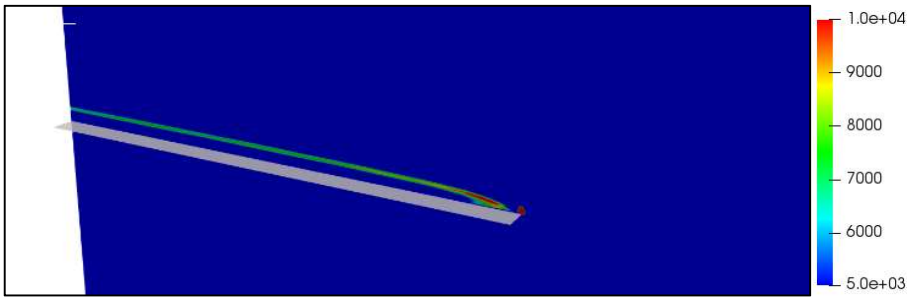
1.0e+04
9000
8000
7000
6000
5.0e+03

(b)

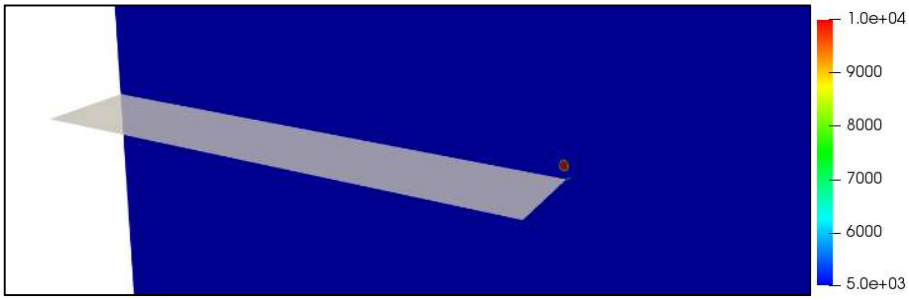
1.0e+04
9000
8000
7000
6000
5.0e+03

(c)

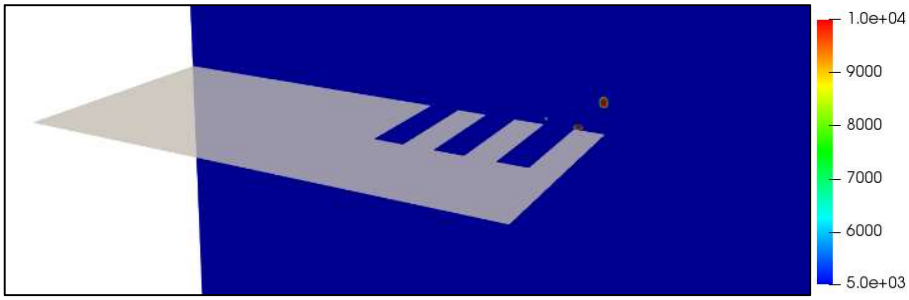

(d)

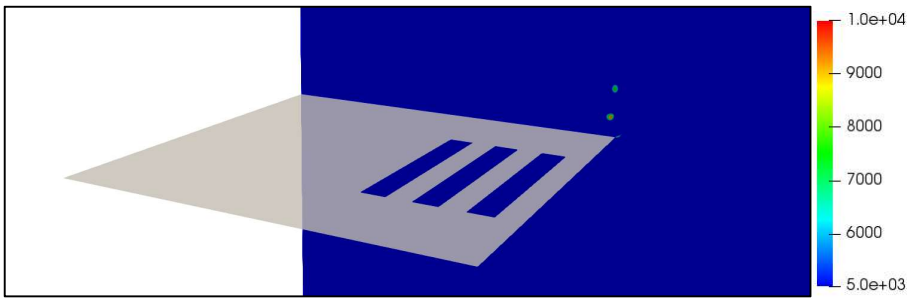

(e)

Figure 42: Contours of vorticity magnitude showing the development of primary wingtip vortex for a flat plate with slits at (a) 0.02c, (b) 0.05c, (c) 0.2c, (d) 0.5c, and (e) 1c from the leading edge

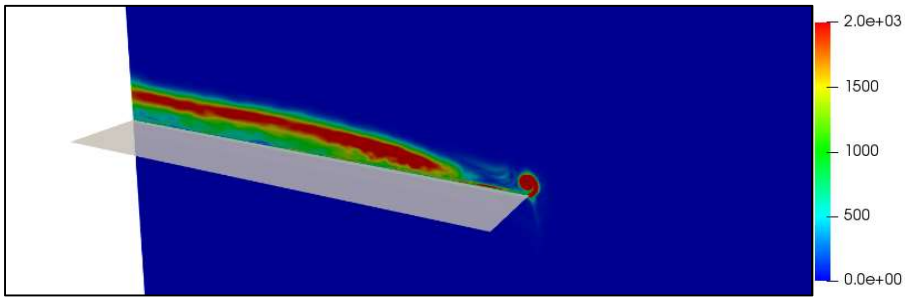

(a)

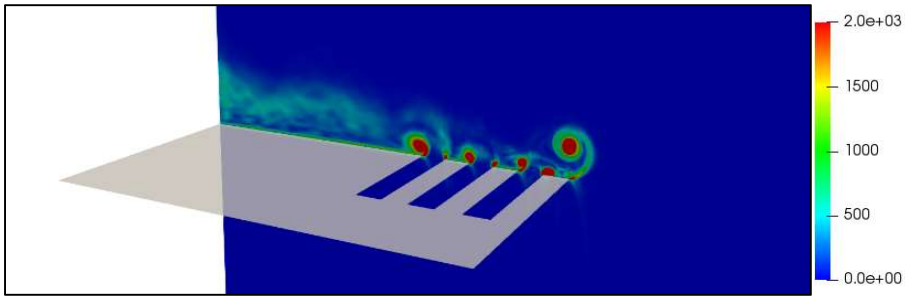

(b)

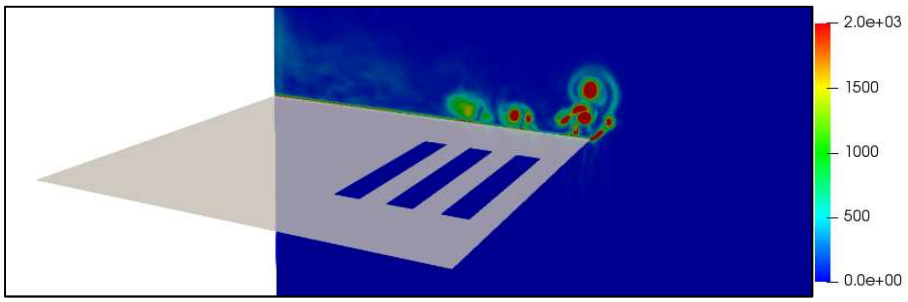

(c)

Figure 43: Contours of vorticity magnitude showing the development of secondary wingtip vortex for a flat plate with slits at (a) 0.2c, (b) 0.6c, and (c) 1c from the leading edge

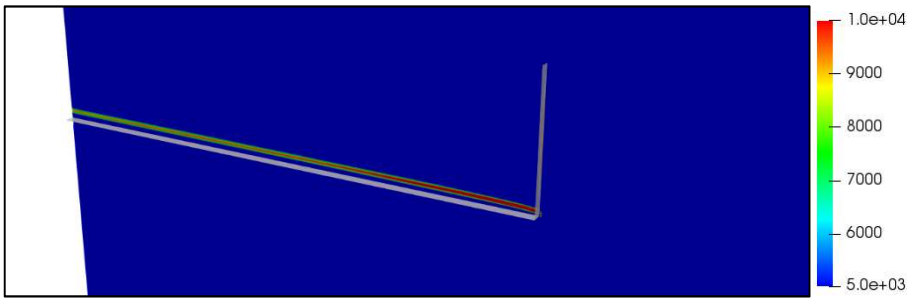

(a)

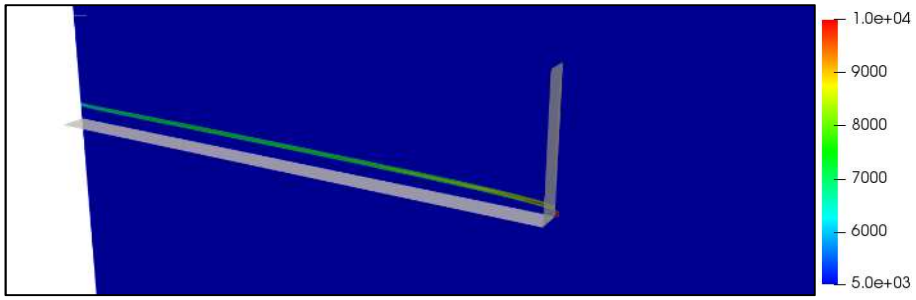

(b)

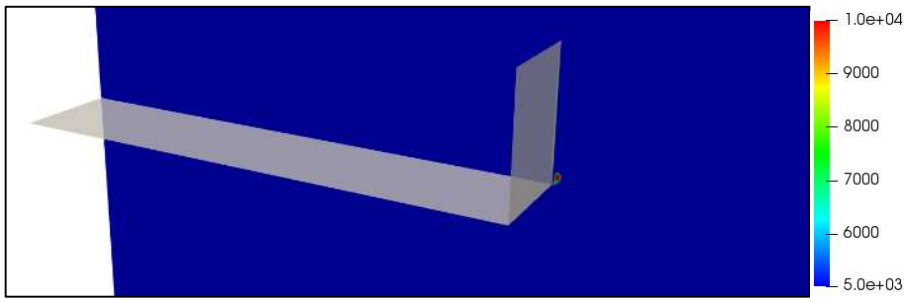

(c)

Figure 44: Contours of vorticity magnitude showing the development of primary wingtip vortex for a flat plate with slits and winglet at (a) 0.05c, (b) 0.02, and (c) 0.2c from the leading edge

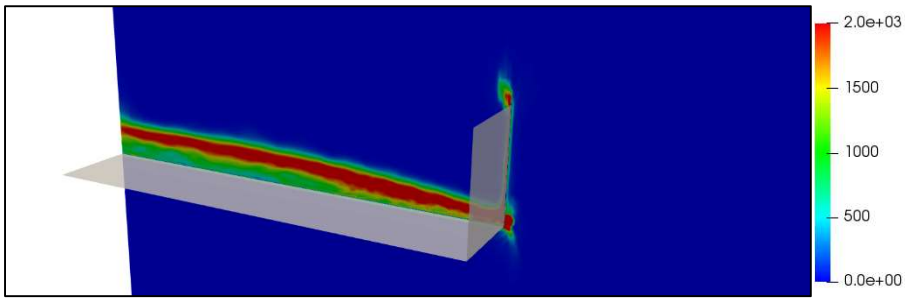

(a)

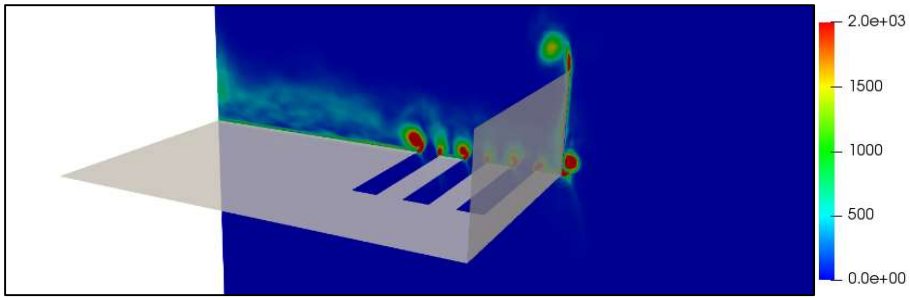

(b)

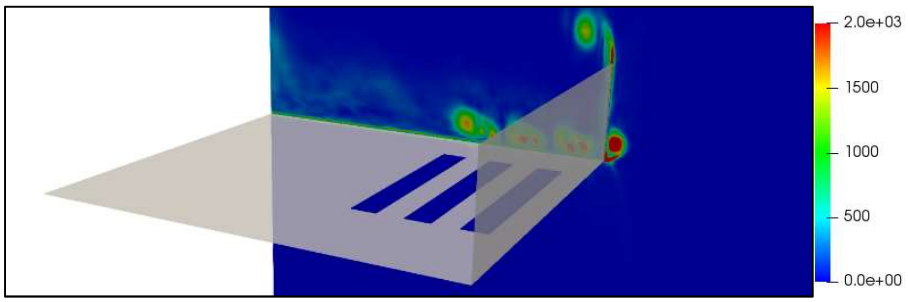

(c)

Figure 45: Contours of vorticity magnitude showing the development of secondary wingtip vortex for a flat plate with slits and winglet at (a) 0.2c, (b) 0.6c, and (c) 1c from the leading edge

6.2.4 Evaluation of Design Effectiveness

The following section evaluates the performance of individual designs against the baseline design.

6.2.4.1 Maximum Streamwise Vorticity

Figure 46 shows variation in maximum mean-vorticity magnitude in the streamwise direction. As suggested by the contours in the previous sections, the introduction of slits reduces vorticity magnitude for the flat plate indicating a relative improvement in performance offered by the introduction of slits.

For the flat plate, the addition of slits introduces complex interactions between the smaller vortices generated at the slits and the larger wingtip vortex. Although this interaction results in an increased vorticity around the leading edge of the airfoil, a rapid reduction in vorticity is observed past 1.25c because of enhanced turbulent diffusion. The addition of winglet alters this flow behavior significantly. The presence of a solid wall between the outer wingtip vortex and the turbulence generated by the slits negatively affects the some of the potential vortex strength mitigation observed for the flat plate with slits. The slits only interact with the upper vortex while the outer vortex at the base of the winglet remains somewhat intact resulting in a reduced overall performance improvement for this design.

Figure 46 (a) and (b) shows increased vorticity magnitude at the leading edge for the airfoil configurations without a winglet. Both these configurations experience a maximum vorticity equal to almost twice the strength of the designs with winglets. Following the leading edge, a sharp decline in vorticity is observed for the flat plate with slits and its maximum vorticity is comparable to the two winglet variants near the trailing edge.

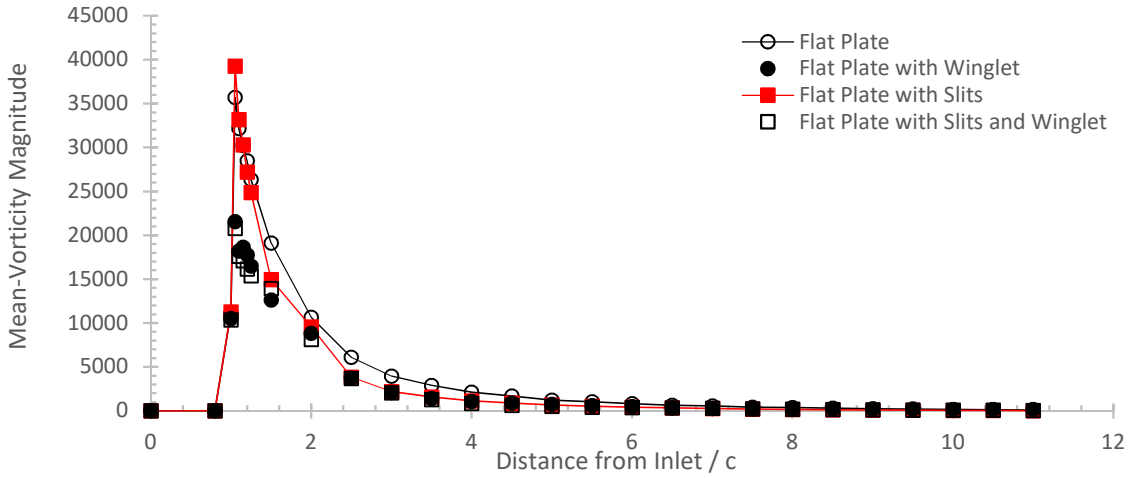

(a)

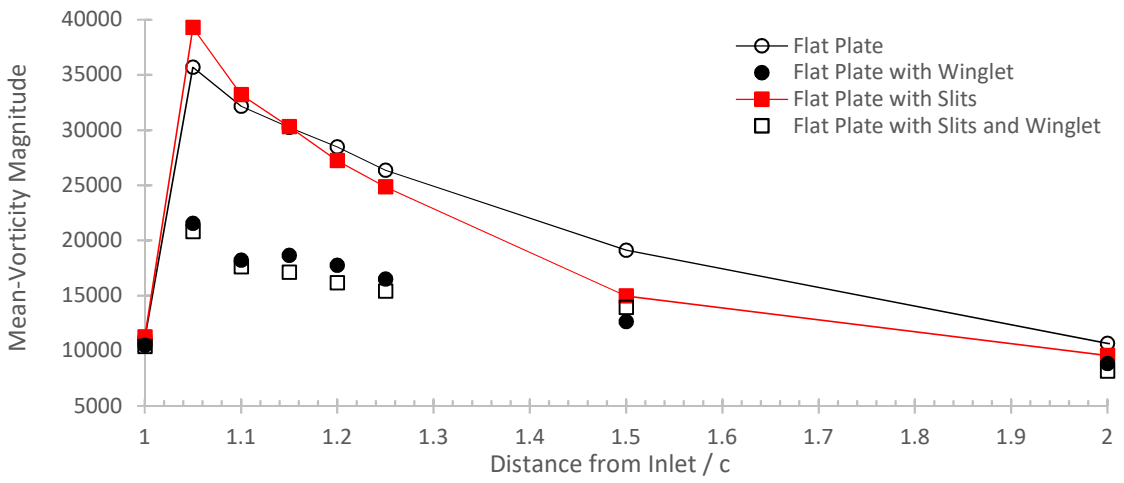

(b)

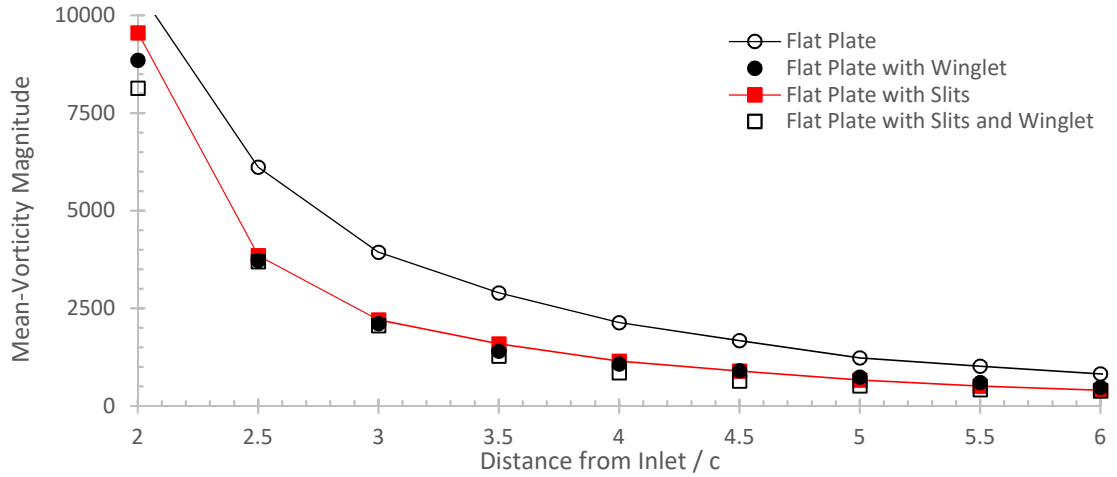

(c)

Figure 46: Distribution of Maximum Mean-Vorticity Magnitude in the streamwise direction (a) throughout the domain, (b) from 1c to 2c, and (c) from 2c to 6c

6.4.2.2 Relative Efficiency

An important metric to validate the accuracy of the numerical simulations was to evaluate the relative efficiency and effectiveness for each of the design. The relative efficiency calculated in this study was based on the lifting forces achieved by each of the designs when compared to the baseline flat plate. Figure 47 shows the relative efficiency of all the airfoils investigated in this study. Unsurprisingly, the addition of a winglet improves aerodynamic efficiency by increasing lift. In a quarterly report in 2009 [6], Boeing announced that their blended winglet design improved aerodynamic efficiency by 4-5% which is qualitatively comparable to the 5.449% and the 6.505% improvement in efficiency reported in the present study. Since the airfoils with slits exhibit enhanced turbulence around the wing, a decrease in efficiency and a loss of lift is somewhat expected. However, it must be remembered that this study only simulates the aerodynamic behavior of a small section of an airfoil near the wingtip. It is expected that performance analysis of a full-scale airfoil with the slits would show a higher relative efficiency than shown in the figure below. Also, the time period of wingtip device operation is also very small. During take-off and landing, almost all present-day wingtip devices exhibit reduced aerodynamic efficiency. For the proposed design, any losses in that short window would potentially be offset by the increased air-traffic as a result of reduced wait times.

$$\text{Relative efficiency} = \frac{F_y \text{ Desig} - F_y \text{ Flat Plate}}{F_y \text{ Flat Plate}} \text{ x } 100 \qquad (22)$$

Design	Relative efficiency for the Coarse Grid	Relative efficiency for the Fine Grid
Flat Plate	NA	NA
Flat Plate with winglet	+ 5.449 %	+ 6.505 %
Flat Plate with slits	- 8.462 %	- 6.378 %
Flat Plate with slits and winglet	- 3.846 %	- 4.273 %

Figure 47: Table containing relative efficiency values

6.4.2.3 Relative Effectiveness

Figure 48 shows the relative effectiveness of the design implementation when compared to its unmodified counterpart. The flat plate with slits shows a 50% reduction in vortex strength till 6c compared to the baseline flat plate while, the flat plate with slits and winglet shows a 30% reduction of vortex strength between 4c-6c. Since cells past 7c get stretched rapidly, it is more appropriate to limit the performance evaluation up to 7c. Overall, both modified design variants show improvements over their baseline counterparts. Although, the winglet design by itself is relatively effective in reducing vortex strength, further study with a full-scale airfoil and with some of the improvements suggested in the previous section will likely show a more substantial improvement of vortex strength reduction.

$$\text{Relative effectiveness} = \frac{\|\omega_{ij}\|\ \text{Baseline} - \|\omega_{ij}\|\ \text{Design}}{\|\omega_{ij}\|\ \text{Baseline}} \text{ x } 100 \qquad (23)$$

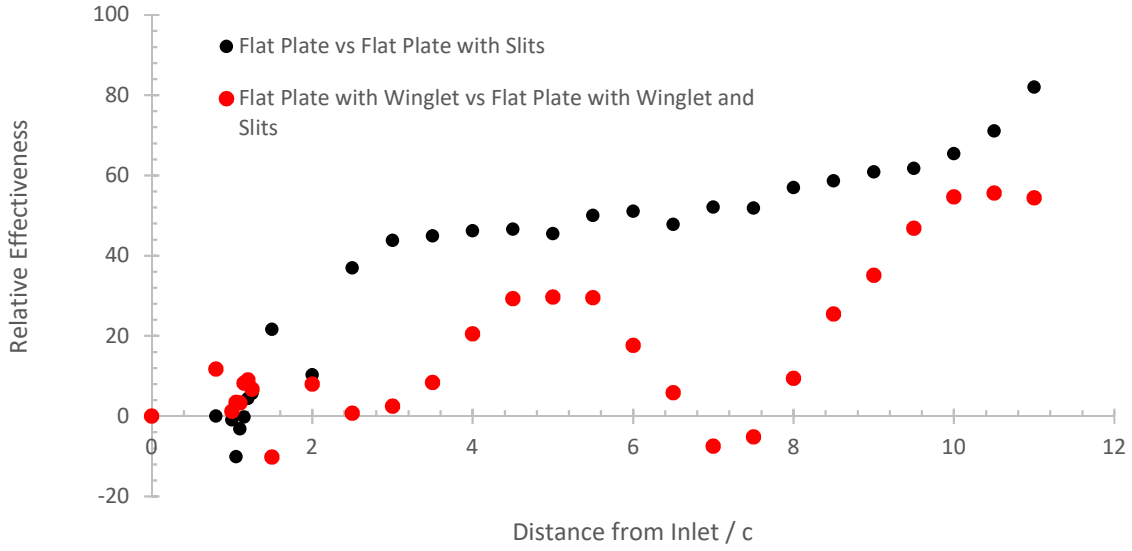

Figure 48: Relative effectiveness

6.2.5 Q-criterion Iso-Volumes

Q-criterion is useful visualization and vortex identification method used frequently in aerospace applications. Defined as the second invariant of the velocity-gradient, Q-criterion describes vortices as regions where vorticity magnitude is greater than the magnitude of rate-of-strain. Equations 24 and 25 describe the mean rate-of-strain and Q criterion.

$$\overline{S_{ij}} = \left(\frac{\partial \bar{U}_i}{\partial x_j} + \frac{\partial \bar{U}_j}{\partial x_i}\right) \tag{24}$$

$$Q - criterion = \frac{1}{2}\left(\|\omega_{ij}\|^2 - \|S_{ij}\|^2\right) \tag{25}$$

Figure 49 shows iso-volumes of Q-criterion colored by mean-vorticity magnitude. According to the figures, the baseline flat plat shows the presence of a single vortex core originating from the leading edge. The introduction of slits shows increased fluctuations around the single vortex with a reduced vorticity magnitude. There is also the presence of complex

turbulence interactions below the vortex throughout the length of the plate. The incorporation of winglets introduces a second vortex which interacts with the primary vortex downstream of the wing. Both winglet variants exhibit similar primary and secondary vortex interaction with the airfoil containing slits showing slightly reduced vorticity on the Q-criterion iso-surfaces. These figures also support the observation that the vortices originate from the leading edge and that the overall structure is still very much intact despite the introduction of the slits and winglets.

Figure 49 also showcases the improvement in flow resolution when compared to the initial simulations using NACA 0012 as shown in Figure 7. Both these images show contours of Q-criterion for a similar range however, the NACA 0012 simulations completely lack the presence of small-scale fluctuations which are shown below.

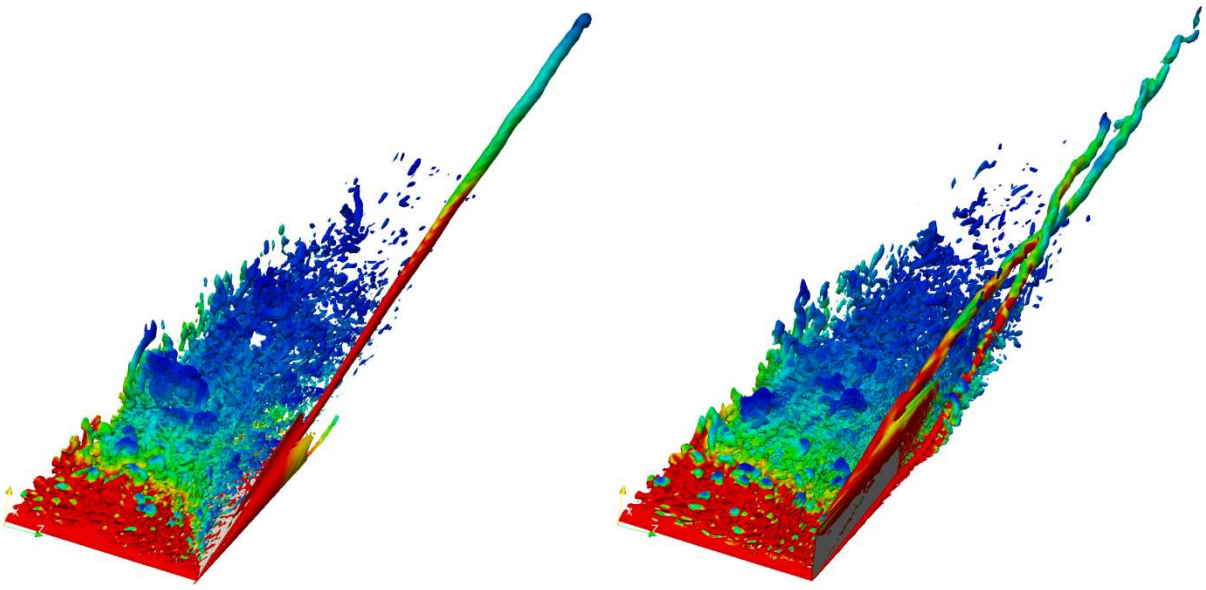

(a) (b)

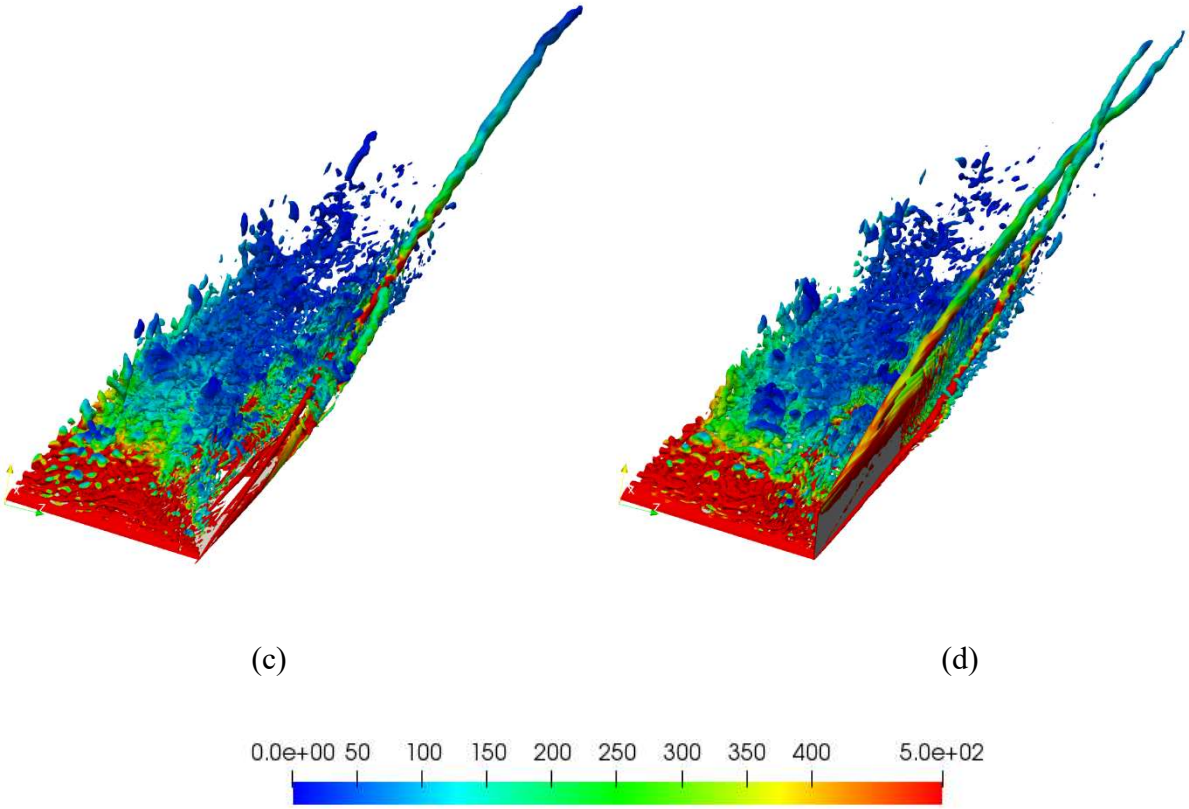

Figure 49: Iso-volumes of Q-criterion colored by mean-vorticity magnitude for the fine grid for a (a) flat plate, (b) flat plate with winglet, (c) flat plate with slits, and (d) flat plate with slits and winglet

6.2.6 Instantaneous Velocity Magnitude Streamlines

Figure 48 shows streamlines of velocity magnitude for all the designs considered in this study. As observed in previous sections, the flat plate designs with modifications and attachments display reduced velocity magnitude in the vortex core accompanied by more diffused and loosely bound wingtip vortex.

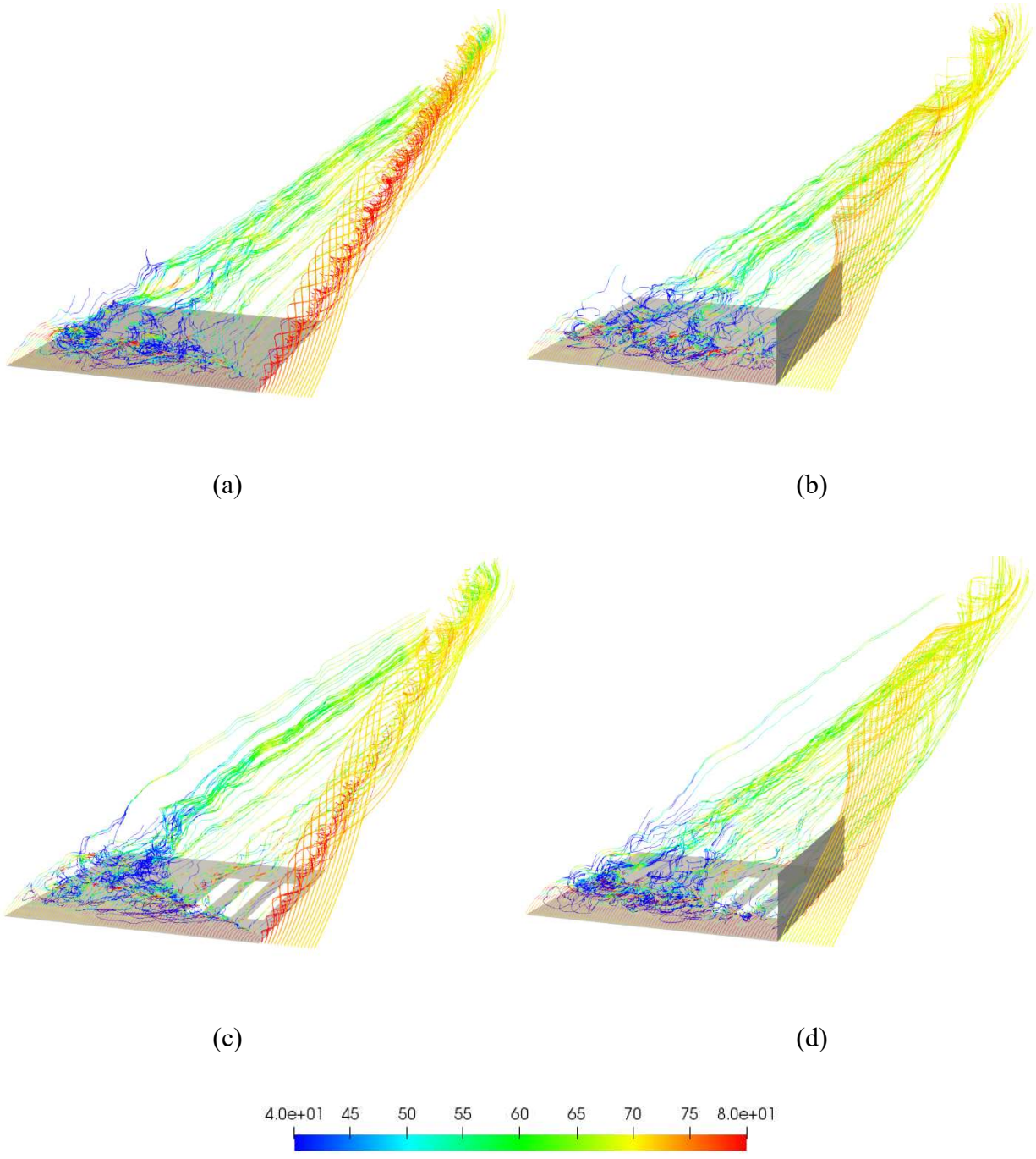

Figure 50: Streamlines of instantaneous-velocity magnitude for the fine grid for a (a) flat plate, (b) flat plate with winglet, (c) flat plate with slits, and (d) flat plate with slits and winglet

CHAPTER VII

CONCLUSIONS AND FUTURE WORK

8.1 Conclusions

Numerical simulations of flow around a NACA 0012 and a flat plate are performed for typical take-off and landing speeds at AoA of 10° using Delayed Detached Eddy Simulation (DDES) and Monotonically Integrated Large Eddy Simulation (MILES). Initial simulations indicated some of the difficulties in grid generation and numerically resolving complex 3D flows with streamwise curvature separated shear layer. Although the simulations with NACA 0012 airfoil using SA-DDES model indicated that the introduction of streamwise slits to bleed air through the airfoil interrupted the formation of a coherent vortex, inaccuracies in numerics and significant increase in predicted aerodynamic losses were observed. To address these issues, a different strategy needed to be adopted. To simplify the grid generation process and to effectively evaluate the proposed wingtip vortex mitigation design, a flat plat with no thickness was used. The lack of curvature ensured that two high resolution structured grids were generated with 10 million and 15 million cells respectively. Numerical simulations were performed using Monotonically Integrated Large Eddy Simulation (MILES) and the Optimization-based Gradient RE-construction (OGRE) low-dissipation scheme for incompressible flow at take-off and landing speeds. Both, the coarse and fine grid results showed the relative merits of using winglets and slits to mitigate wingtip vortices. The proposed design showed a decline in vorticity magnitude in the streamwise direction via increased turbulent diffusion. Although a decrease in aerodynamic lift was observed for the proposed design, the reduced wait times and increased air-traffic would potentially offset the decrease in efficiency. Results also indicated that the mechanism of vortex generation is initiated at the leading edge and perhaps future designs should use a leading-edge targeted design

optimization rather than making changes to existing winglet design or airfoil structure. Hence it can be concluded that although the proposed design mitigates vortex strength when compared to the baseline airfoils and airfoils with winglets, modifications to leading edge design would further improve the performance of the proposed design in mitigating wingtip vortex strength.

8.2 Future Work

Future efforts will focus on the design and implementation of a new leading-edge design combined with the slit design investigated in this study. Another avenue for investigation would be to determine the vortex termination length via numerical simulation using an extended domain to better understand the vortex diffusion process and for comparisons with experimentally available data.

LIST OF REFERENCES

[1] Panagiotou P., Kaparos P., Yakinthos K., “Winglet design and optimization for a MALE UAV using CFD”, Aerosp. Sci. Technol. 2014, 39, 190–205.

[2] FAA Order JO 7110.65U, 9 February 2012, p. PCG A−6 (http://www.faa.gov/documentLibrary/media/Order/ATC.pdf).

[3] Phelps, M, “Revised Wake Turbulence Categories Increase Airport Capacity”, Flying, Published online January 31, 2013. (http://www.flyingmag.com/news/revised-wake-turbulence-categories-increaseairport-capacity

[4] Croft, J., "In The Wake of An A380: Dealing With Wake Turbulence". Aviation Week Network.

[5] Graham, "Flight from Los Angeles sent into nosedive for 10 seconds after hitting vortex”, report, news.com.au.

[6] Freitag, W., Schulze, T.E., “Blended Winglets Improve Performance”, Boeing AERO Quarter 03 Report 2009

[7] Illinois Aviation Hall Of Fame, William E. "Billie" Somerville 1869-1950.

[8] Joseph R. Chambers, "Winglets". Concept to Reality: Contributions of the Langley Research Center to US Civil Aircraft of the 1990s (PDF). NASA Langley Research Center. p. 35. ISBN 1493656783.

[9] James C. Patterson Jr., “Vortex Attenuation Obtained in the Langley Vortex Research Facility”, Journal of Aircraft 1975 12:9, 745-749

[10] Hubert C. Smith, “Method for reducing the tangential velocities in aircraft trailing vortices”, Journal of Aircraft 1980 17:12, 861-866

[11] E. Anderson, C. Wright, and T. Lawton, “Experimental study of the structure of the wingtip vortex”, 38th Aerospace Sciences Meeting and Exhibit. January

[12] Guha, T. K., “Active Control Of Wingtip Vortices Using Piezoelectric Actuated Winglets”, Florida State University, 2017.

[13] Altaf, A., “Wingtip Vortex Alleviation Using a Reverse Delta Type Add-on Device”, International Journal of Aviation, Aeronautics, and Aerospace, (3). https://doi.org/10.15394/ijaaa.2017.1178

[14] Jean-Eloi W. Lombard, David Moxey, Spencer J. Sherwin, Julien F. A. Hoessler, Sridar Dhandapani, and Mark J. Taylor, “Implicit Large-Eddy Simulation of a Wingtip Vortex”, AIAA Journal 2016 54:2, 506-518

[15] Jamal T., Walters D., Chitta V., (2017), “3D Simulation of Flow in a Vortex Cell Using RANS and Hybrid RANS-LES Turbulence Models,” ASME International Mechanical Engineering Congress and Exposition, Volume 7:Fluids Engineering():V007T09A061. doi:10.1115/ IMECE2017-70599.

[16] Ringleb, F.O., “Separation control by trapped vortices”. In: Lachmann GV (ed) Boundary layer and flow control. Pergamon Press, Oxford

[17] Splalart, P.R., and Allmaras, S.R., “ A One-Equation Turbulence Model for Aerodynamic Flows”, AIAA paper 92-0439.

[18] P. R. Spalart, S. Deck, M. L. Shur, K. D. Squires, M. Kh. Strelets, and A. Travin, “ A New Version of Detached-eddy Simulation, Resistant to Ambiguous Grid Densities “,Theoret. Comput. Fluid Dynamics (2006) 20: 181.

[19] Spalart, Philippe & Jou, W-H & Strelets, Michael & Allmaras, Steven. (1997). Comments on the Feasibility of LES for Wings, and on a Hybrid RANS/LES Approach.

[20] Fureby, C., & Grinstein, F. (1999). Monotonically integrated large eddy simulation of free shear flows. AIAA Journal,37, 544-556. doi:10.2514/3.14208

[21] Poe, N.M.W., Walters, D.K., Luke, E.A., and Morris, C.I., 2015. “A low-dissipation second-order upwind flux formulation for simulation of complex turbulent flows”. Proceedings of the ASME International Mechanical Engineering Congress & Exposition, Houston, TX, November 13-19.

[22] ANSYS, ANSYS Fluent Theory Guide 14.5.7, ANSYS, Inc., Canonsburg, PA.

[23] ParaView: An End-User Tool for Large Data Visualization, Visualization Handbook, Elsevier, 2005, ISBN-13: 978-0123875822.